RESEARCH ARTICLE

WILEY

Geochronology and geochemistry of a newly identified Permian hornblende gabbro suite in Aqishan–Yamansu Belt, eastern Tianshan, NW China: Implications on petrogenesis and tectonic setting

Hongjun Jiang[1,2,3] | Huayong Chen[1,4,5] | Lin Gong[1,2] | Shuanliang Zhang[1,2] | Gaobin Chu[1,2] | Yumin Ai[1,2]

[1]Key Laboratory of Mineralogy and Metallogeny, Guangzhou Institute of Geochemistry, Chinese Academy of Sciences, Guangzhou, China

[2]University of Chinese Academy of Sciences, Beijing, China

[3]Geological Party No. 214, China-Shaanxi Nuclear Industry Group, Xi'an, China

[4]CAS Center for Excellence in Deep Earth Science, Guangzhou, China

[5]Guangdong Provincial Key Laboratory of Mineral Physics and Materials, Guangzhou, China

Correspondence
Huayong Chen, Key Laboratory of Mineralogy and Metallogeny, Guangzhou Institute of Geochemistry, Chinese Academy of Sciences, Guangzhou 510640, China.
Email: huayongchen@gig.ac.cn

Permian mafic-ultramafic intrusions have great significance for understanding the geodynamic evolution of the Late Palaeozoic eastern Tianshan Orogen due to containing important information on the nature of mantle sources, crust–mantle interaction, and magmatic differentiation. Increasingly, more Permian mafic-ultramafic intrusions are discovered in the Jueluotage belt, especially in the Kangguer ductile shear zone, whereas the mafic-ultramafic intrusions in the Aqishan–Yamansu belt are ill-informed. In this study, we provide zircon U–Pb geochronological, geochemical, and Sr–Nd–Pb–Hf isotopic data of a newly identified hornblende gabbro suite at the Shaquanzi Fe–Cu deposit in the Aqishan–Yamansu Belt. Zircon U–Pb dating results indicate that the Shaquanzi hornblende gabbro was emplaced at Early Permian (ca. 274–265 Ma). The rocks are calc-alkaline and have arc-like geochemical features, including enrichments in large-ion lithophile elements (LILEs: Rb, Ba, K, Pb and Sr) and light rare-earth elements (LREEs: Nb, Ta, Zr, Hf, and Ti), and depletions in high-field-strength elements (HFSEs) with markedly negative Nb and Ta anomalies. The rocks also exhibit depleted-mantle isotopic signatures, with positive bulk-rock $\varepsilon_{Nd}(t)$ values of +3.34 to +4.44 and positive zircon $\varepsilon_{Hf}(t)$ values of $+2.8 - +8.7$, which are relatively more enriched than those of coeval mafic-ultramafic intrusions from the Kangguer ductile shear zone, but similar to those in the Central Tianshan Massif. We suggest that the Shaquanzi mafic intrusion suite was generated by 10–30% partial melting of a depleted-mantle source at over 85 km depth, corresponding to the garnet to garnet-spinel stability field. And the mantle source had likely been metasomatized by slab-derived fluids of previous subduction. Integrating with geochemical data of the coeval mafic-ultramafic and felsic intrusive rocks in the adjacent tectonic belts of eastern Tianshan Orogen, we speculate that the Shaquanzi mafic intrusion was formed in a post-collision extensional setting, probably triggered by slab breakoff. Metasomatism of the depleted lithospheric mantle had likely occurred during the pre-Permian subduction of the Kangguer oceanic slab.

KEYWORDS
Aqishan–Yamansu Belt, early Permian, eastern Tianshan, petrogenesis, post-collisional extension, Shaquanzi hornblende gabbro

1 | INTRODUCTION

The eastern Tianshan forms an important part of the Central Asian Orogenic Belt (CAOB), situating between the Junggar Block to the north and Tarim Block to the south (Şengör, Natal'In, & Burtman, 1993). Numerous mafic-ultramafic intrusions have been recovered in this domain and some of them are closely associated with magmatic Cu–Ni sulphide deposits, such as the newly discovered Baixintan and Lubei, and the well-known Baishiquan, Xiangshan, and Huangshan. This has attracted many studies on the nature and tectonic setting of these mafic-ultramafic intrusions (e.g., B. Y. Chen, Yu, & Liu, 2018; Deng et al., 2020; Gao et al., 2013; Gao & Zhou, 2013; J. W. Mao et al., 2008; Y. J. Mao, Qin, Li, & Tang, 2015; Y. J. Mao, Qin, Tang, Feng, & Xue, 2016; Qin et al., 2011; Su et al., 2011, 2012; T. Sun et al., 2013a; T. Sun, Qian, Li, Xia, & Yang, 2013b; Y. Zhao, Xue, Zhao, Yang, & Ke, 2015; M. F. Zhou, Lesher, Yang, Li, & Sun, 2004). Published age data indicate that they were mostly formed within a narrow Early Permian (301–265 Ma) age interval, with the exceptions of the Ordovician–Carboniferous Xiadong (479–313 Ma; Su et al., 2014), Heishanxia (423.7 Ma; Su et al., 2011), Hulu (388.6–377 Ma; Zhao, Xue et al., 2018a), Sidingheishan (365 Ma; Su et al., 2011), and Tulaergen (357.5 Ma; San et al., 2010). Moreover, these intrusions exhibit geochemical signatures of arc, and positive $\varepsilon_{Hf}(t)$ and $\varepsilon_{Nd}(t)$ values, relatively wide $(^{87}Sr/^{86}Sr)_i$ range, suggesting a metasomatized mantle source with a certain degree of contamination by juvenile arc crust and/or ancient Central Tianshan crust (e.g., Deng et al., 2015; Y. J. Mao et al., 2016; Y. Sun et al., 2019; D. Tang et al., 2013). However, there is still no consensus on the actual geodynamic setting, with proposals mainly focused around arc-related Alaskan-type zoned intrusive complexes (e.g., C. Han et al., 2010, 2013a), post-collisional extension and Tarim mantle plume-related (e.g., Su et al., 2011; D. Tang et al., 2013; M. F. Zhou et al., 2004), or asthenospheric upwelling triggered by post-collisional slab breakoff and/or delamination of the thickened crust (e.g., Song et al., 2011).

These Permian mafic-ultramafic intrusions generally occur along sub-parallel trans-lithospheric faults, mainly in the Kangguer ductile sheer zone and minor in the Dananhu–Tousuquan island arc belt, and Central Tianshan Massif (Li, Wang, et al., 2019a; Shi et al., 2021). Nevertheless, no such intrusions had been found in the Aqishan–Yamansu Belt, which is also an important tectono-metallogenic belt in the eastern Tianshan (e.g., J. S. Han et al., 2019), until hornblende gabbro was reported in the Shaquanzi Fe–Cu deposit in recent years (Jiang et al., 2018). However, the emplacement age and petrogenesis of the hornblende gabbro remain poorly understood, and thus little implications can be deduced on the regional tectonic evolution and ore-forming potential of the Aqishan–Yamansu Belt. This study aims to better understand the Shaquanzi mafic intrusion through presenting a detailed account on its geology, age, geochemical, and Sr–Nd–Pb–Hf isotopic features. We then provided a synthesis of a large dataset on whole-rock Sr–Nd isotopes (n = 139), and zircon U–Pb age (n = 50) and Hf isotopes (n = 167) from the adjacent mafic-ultramafic intrusions in the various eastern Tianshan magmatic belts to constrain the source nature and tectonic evolution of the Early Permian mafic-ultramafic magmatism in the eastern Tianshan Orogen.

2 | GEOLOGICAL SETTING

The CAOB is the world's largest Phanerozoic accretionary orogen and separates the Siberian Craton to the north and the Sino–Korean and Tarim cratons to the south (Figure 1a; W. Xiao, Windley, Allen, & Han, 2013; W. Xiao et al., 2014, 2015; Windley, Alexeiev, Xiao, Kröner, & Badarch, 2007). The Chinese Tianshan Orogen is located in the southern part of CAOB and formed by prolonged accretion/collision of island arc terranes, micro-continental fragments, oceanic crust remnants, and accretionary wedges (Figure 1b; Charvet et al., 2007; Jahn, Wu, & Chen, 2000). From north to south, the Chinese eastern Tianshan can be separated into three tectonic belts, including Bogeda–Haerlike belt, Jueluotage belt, and Central Tianshan Massif, by the approximately E-W-trending southern margin Fault of Turpan Basin and Aqikekuduke–Shaquanzi Fault (Figure 1c; D. Tang et al., 2013; Zhao et al., 2018b). The Jueluotage belt consists of (from north to south) the Dananhu–Tousuquan island arc, Kangguer ductile shear zone, and the Aqishan–Yamansu belt, which are divided by the Kangguer and Yamansu crustal scale faults, respectively (Figure 1c; Su et al., 2011). The Dananhu–Tousuquan island arc mainly comprises Ordovician–Carboniferous volcanic and intrusive rocks and is famous for hosting important Tuwu–Yandong porphyry copper deposit (B. Xiao et al., 2017). The Kangguer ductile shear zone mainly contains volcaniclastic rocks and greenschist-facies metamorphosed Carboniferous ophiolitic, with outcrop of numerous Permian mafic-ultramafic intrusions and minor felsic intrusions (W. Q. Li, Dong, & Zhou, 2000; J. Mao et al., 2005; Qin et al., 2002; W. J. Xiao, Zhang, Qin, Sun, & Li, 2004). It also hosts some important gold (e.g., Shiyingtan and Kangguer; Jiang et al., 2018) and Cu–Ni (e.g., Xiangshan and Huangshna; Qin et al., 2002) deposits. The Aqishan–Yamansu Belt, restricted by the Yamansu and Aqikekuduke–Shaquanzi faults and located to the north of the Central Tianshan Massif, is mainly composed of Carboniferous volcanic and volcaniclastic rocks, together with many Carboniferous–Permian granitoids (Jiang et al., 2017; L. Zhao, Chen, Hollings, & Han, 2019a, 2019b; T. F. Zhou et al., 2010). This belt is also well-known for hosting many Fe (–Cu) deposits, e.g., the Yamamsu, Bailingshan, Chilongfeng Fe deposits (W. Zhang et al., 2018), and the Heijianshan, Duotoushan, and Shaquanzi Fe–Cu deposits (F. Liu, Chai, Li, & Yang, 2019).

In the Jueluotage belt, there are many mafic-ultramafic intrusions located in the eastern part of Kangguer ductile shear zone, and also locally in the Central Tianshan Massif (Figure 1c). Recent studies also documented mafic-ultramafic intrusions in the Dananhu–Tousuquan island arc (Yueyawan, Lubei, and Baixintan; B. Y. Chen et al., 2018; B. Chen, Yu, Liu, & Tian, 2019; Y. Sun et al., 2019; G. C. Zhou et al., 2019). The majority of these mafic-ultramafic intrusions are associated with Ni–Cu sulphide mineralization, such as Huangshan, Huangshandong, Xiangshan, Tianyu, Baishiquan, Lubei, and Yueyawan, forming a number of important Ni–Cu sulphide ore belts,
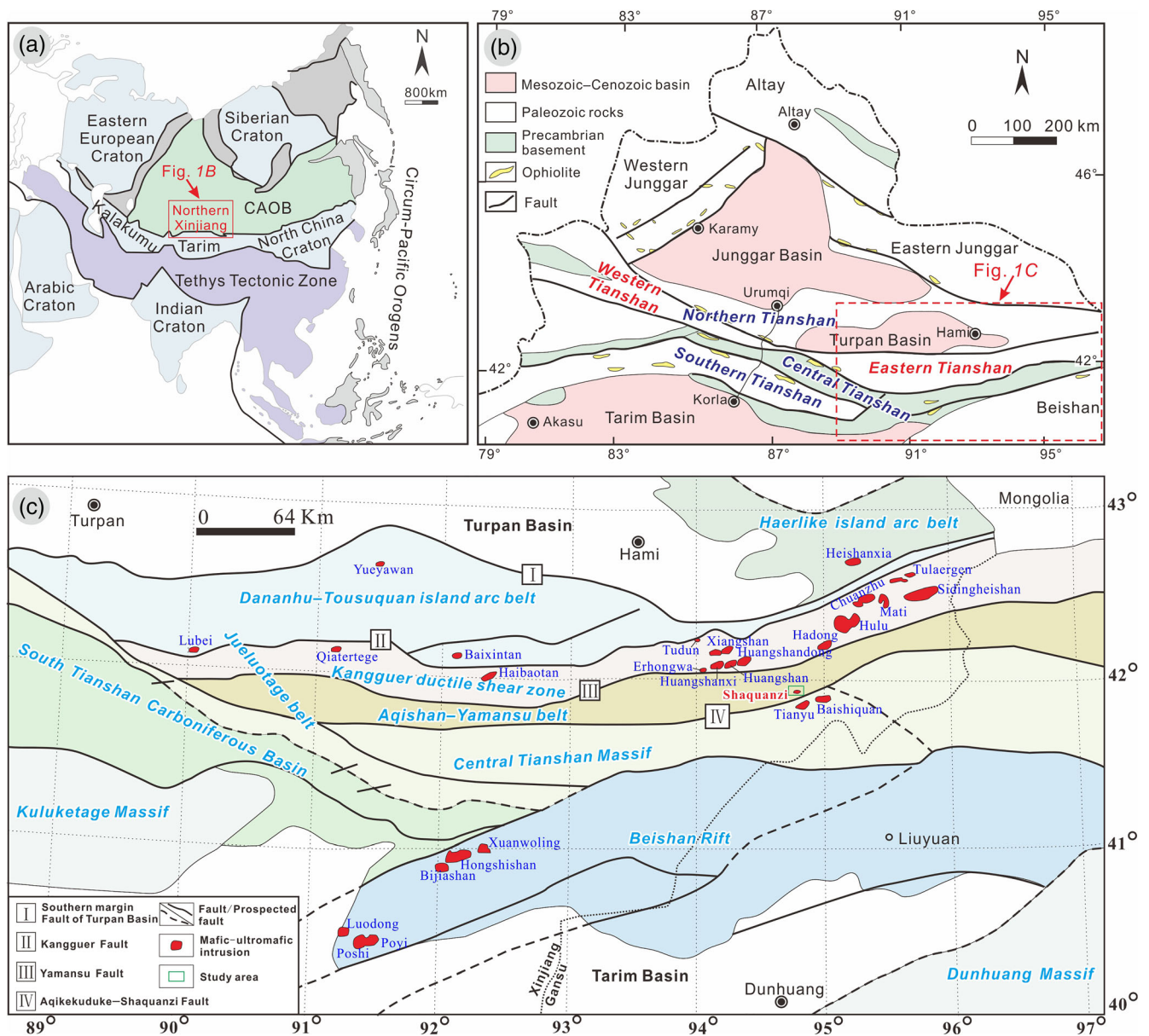
FIGURE 1 (a) Simplified tectonic map showing the location of the Central Asian Orogenic Belt (CAOB), modified after Şengör (1993); (b) Tectonic map of northern Xinjiang, showing the location of the eastern Tianshan Orogen, modified after Y. J. Chen, Pirajno, Wu, Qi, and Xiong (2012); (c) Geologic map of the eastern Tianshan and mafic-ultramafic intrusion distributions, modified after Su et al. (2011)

including the Huangshan–Jing'erquan, Baixintan–Lubei, and Tianyu–Baishiquan (Qin et al., 2012; G. C. Zhou et al., 2019). This makes northern Xinjiang the second most important Ni province in China (Song & Li, 2009).

3 | REGIONAL GEOLOGY AND PETROGRAPHY

The Shaquanzi Fe–Cu deposit, situated at the eastern Aqishan–Yamansu Belt, contains a reserve of 2.49 million tonnes (Mt) Fe @ 26–49%, and 2040 t Cu @ 0.23–1.58% (Jiang et al., 2018). The orebodies are mainly hosted in the Upper Carboniferous Shaquanzi

Formation andesite and volcaniclastic rocks (328–303 Ma; F. Liu et al., 2019). Intrusive rocks at Shaquanzi include granite porphyry, porphyritic diorite, diorite dike (276.3 ± 1.4 Ma; F. Liu et al., 2019), diorite (298.5 ± 5.1 Ma; Jiang et al., 2017), and hornblende gabbro, all intruding into the Shaquanzi Formation.

The Shaquanzi hornblende gabbro outcrops occupy about 25% of the ore district, especially in its middle part (Figure 2). These rocks are massive and coarse- to medium-grained (Figure 3a,c). The hornblende gabbro mainly contains plagioclase (45–50 vol%), hornblende (35–45 vol%), clinopyroxene (5–10 vol%), and minor magnetite (<5 vol%). Some samples are slightly altered, as manifested by sericitization in the plagioclase, and chloritization along the hornblende, and clinopyroxene grain margin (Figure 3b,d).
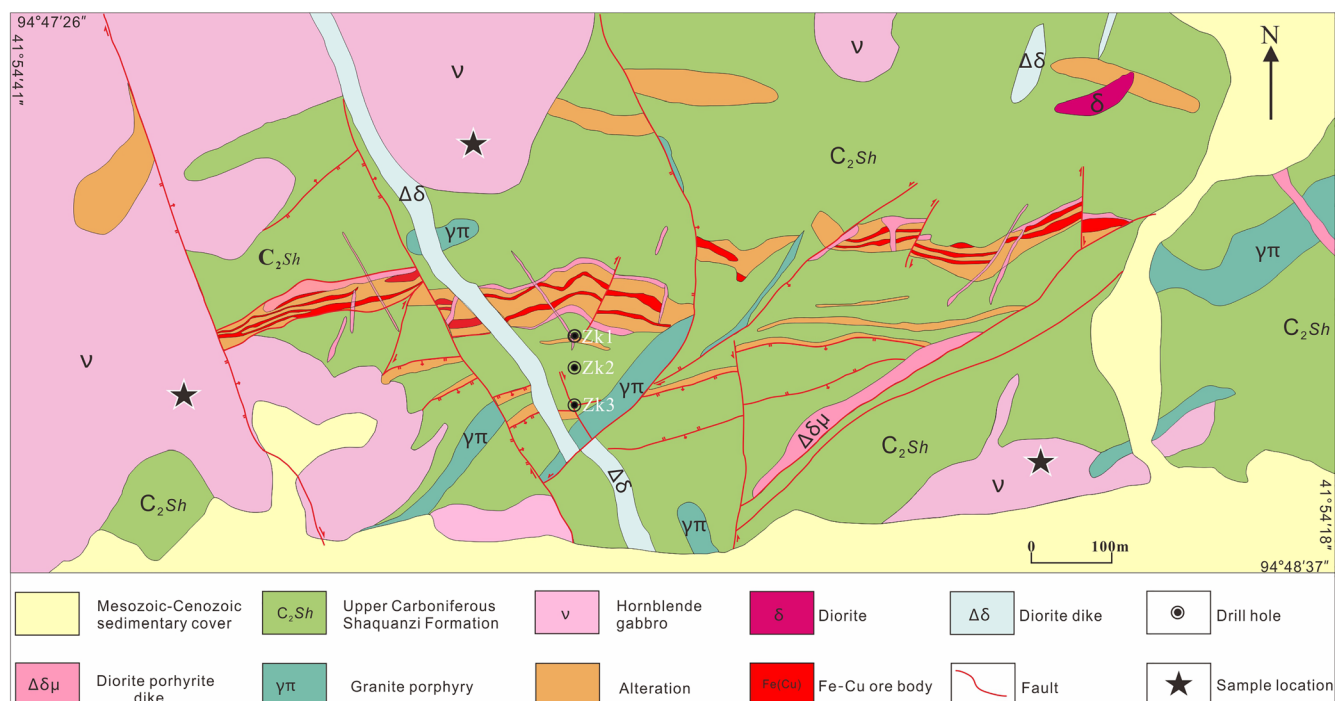
FIGURE 2 Geologic map of middle ore section in the Shaquanzi Fe–Cu deposit, modified after Jiang et al. (2018)

FIGURE 3 Hand specimen photos and petrographic microphotographs (cross-polarized light) of the Shaquanzi gabbro. Chl, chlorite; Cpx, clinopyroxene; Hb, hornblende; Mt, magnetite; Pl, plagioclase
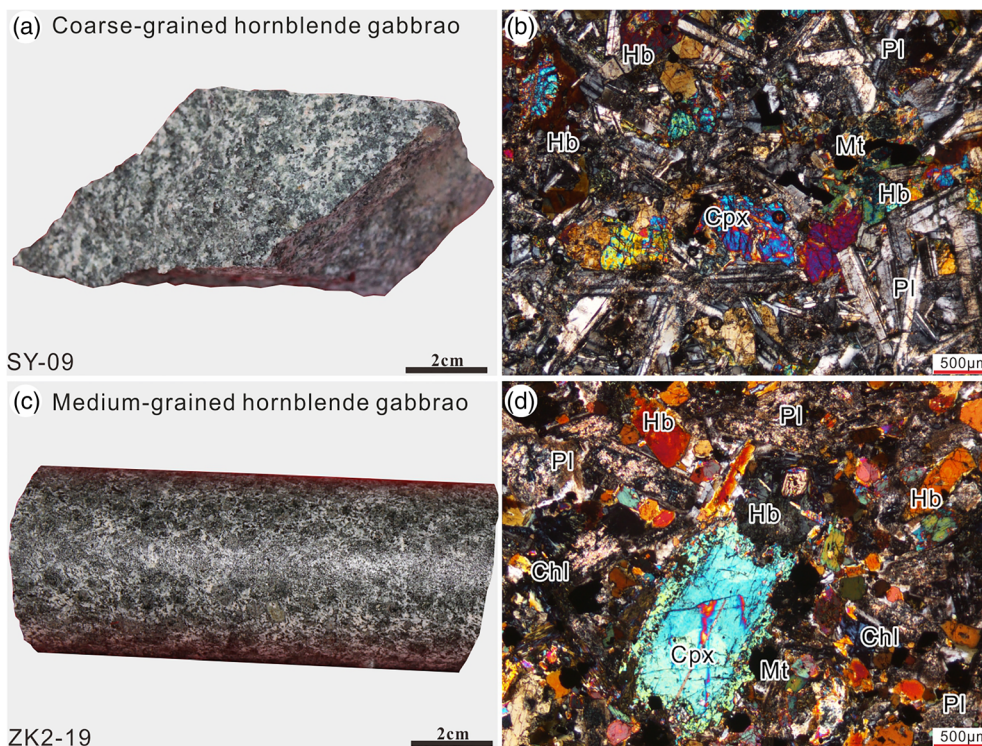
4 | ANALYTICAL METHODS

4.1 | Zircon U–Pb–Hf isotope analyses

Zircon grains were separated from two Shaquanzi hornblende gabbro samples (SY-09:41°54′23″N, 94°48′21″E and ZK2-19:41°54′28″N, 94°47′56″E) by conventional density and magnetic separation techniques before being selected under a binocular microscope. Zircon CL images were carried out to observe the zircon internal structures, using a JXA-8100 Electron Probe Microanalyser with a Mono CL3 Cathodoluminescence System at the Guangzhou Institute of Geochemistry, Chinese Academy of Sciences (GIGCAS).

Zircon trace element analyses and U–Pb dating for the inclusion-free and least-fractured zircon crystals were conducted simultaneously using an Agilent 7500a ICP-MS coupled with a 193 nm ArF excimer laser ablation system at the GIGCAS. A repetition rate of 8 Hz and constant energy of 80 mJ were used with a 31 μm spot size. The external standards are NIST SRM 610 glass and Temora zircon (Black et al., 2003; Pearce et al., 1997). Every five sample analyses were followed by analysis of two Temora zircon standards. The Temora zircon yielded a weighted mean $^{206}Pb/^{238}U$ age of 416.9 ± 2.4 Ma (1σ; n = 26), which is consistent with recommended value (Black et al., 2003). Detailed analytical procedures were same as C. Y. Li et al. (2012). ICP-MS Data Cal software was used to reduce the U–Pb isotopic data (Liu et al., 2010). Plotting of concordia diagrams and weighted mean age calculations were constructed using the programme Isoplot/Ex_ver3 (Ludwig, 2003).

Zircon Lu–Hf isotopic analyses were carried out using a Neptune MC-ICP-MS, equipped with 193 nm ArF excimer laser ablation system at GIGCAS. Detailed analytical procedures and working conditions are given by G. J. Tang et al. (2012). Ten dated zircon grains of sample SY-09 were selected for analysis, with Penglai zircon as the external standardization. The obtained weighted mean $^{176}Hf/^{177}Hf$ ratio of Penglai zircon grains is 0.282876 ± 0.000010 (2σ, n = 6), which was consistent with the recommended values within 2σ (X. H. Li et al., 2010). The measured isotopic ratios of $^{176}Hf/^{177}Hf$ were normalized to $^{179}Hf/^{177}Hf$ = 0.7325. The initial $^{176}Hf/^{177}Hf$ ratios were calculated by the ^{176}Lu decay constant reported by Söderlund, Patchett, Vervoort, and Isachsen (2004) and the measured $^{176}Lu/^{177}Hf$ ratios. The $ε_{Hf}(t)$ values were calculated by using Chondritic values of $^{176}Hf/^{177}Hf$ = 0.0336 and $^{176}Lu/^{177}Hf$ = 0.282785 recommended by Bouvier, Vervoort, and Patchett (2008). Single-stage Hf model ages (T_{DM1}) were calculated assuming the parental magma is directly derived from the depleted mantle, which has linear isotopic growth from $^{176}Hf/^{177}Hf$ = 0.279718 (4.55 Ga) to 0.283250 (present), with $^{176}Lu/^{177}Hf$ = 0.0384 (Griffin et al., 2000).

4.2 | Whole-rock major and trace element analyses

Seven least altered hornblende gabbro samples were selected for whole-rock major and trace elements analysis by X-ray fluorescence spectrometry (XRF) and inductively coupled plasma-mass spectrometry (ICP-MS) at the ALS Chemex Company in Guangzhou, China. Samples were first powdered to below 200 mesh and then fluxed with lithium borate flux (50%–50% $Li_2B_4O_7$–$LiBO_2$) to make homogeneous flat molten glass discs at 1,050–1,100°C. The major elements were then analysed by XRF with these glass discs. The analysis precision for major elements is better than 1%. For trace elements, including rare-earth elements (REEs), about 50 mg aliquots of powder were mixed well with lithium metaborate flux, and then fused in a furnace at 1,000°C. Before being analysed by ICP-MS, the molten product was then cooled and dissolved in 100 ml of 4% HNO_3. The analytical precision for most trace elements was better than ±5%.

4.3 | Whole-rock Sr–Nd–Pb isotope analyses

Three hornblende gabbro samples were selected for Sr–Nd–Pb isotopic analyses by using a Micromass Isoprobe multi-collector ICP-MS at the State Key Laboratory of Isotope Geochemistry, GIGCAS. Details of Sr–Nd–Pb isotope analytical procedures were as described by Zhang, Chen, et al. (2016a) and Y. G. Xu, Zhang, Qiu, Ge, and Wu (2012). The normalizing parameter used to correct the measured Sr and Nd isotopic ratios are $^{86}Sr/^{88}Sr$ = 0.1194 and $^{146}Nd/^{144}Nd$ = 0.7219, respectively. Analyses of standards NBS987 and Jndi-1 over the measurement period provided $^{87}Sr/^{86}Sr$ = 0.710289 ± 0.000007 (2σ), and $^{143}Nd/^{144}Nd$ = 0.512095 ± 0.000004 (2σ), respectively. Analyses of standard NBS981 during the analysis period yielded $^{206}Pb/^{204}Pb$ = 16.9319 ± 0.0003, $^{207}Pb/^{204}Pb$ = 15.4849 ± 0.0003, and $^{208}Pb/^{204}Pb$ = 36.6781 ± 0.0009. All these ratios are within the errors of recommended values (Jochum et al., 2005). The bulk-rock initial isotopic ratios of the samples were calculated based on their respective zircon U–Pb ages.

5 | RESULTS

5.1 | Zircon U–Pb ages and Ti-in-zircon thermometer

Sample SY-09 and ZK2-19 were zircon U–Pb dated. Zircon grains recovered from these hornblende gabbro rocks are dark grey to colourless, with lengths of 55–155 μm and length/width ratios ranging from 1 to 4. Zircons from sample SY-09 are larger than those from ZK2-19. Both of them are subhedral to anhedral and columnar, showing linear zoning (Figure 4). Most zircon grains have similar geochemical characteristics, displaying distinct positive Ce and negative Eu anomalies, and featured by LREE depletions and HREE enrichments on chondrite-normalized patterns, which are all typical of igneous zircons (Hoskin & Schaltegger, 2018). Concentrations of Th and U in these zircons vary from 42 to 8,256 ppm and from 112 to 2,798 ppm, respectively, with high Th/U ratios of 0.37–8.12, suggesting a magmatic origin (Koschek, 1993) (Table 1).

Sample SY-09 (Figure 3a,b) defined a weighted mean $^{206}Pb/^{238}U$ age of 265.4 ± 2.2 Ma (Figure 4a; MSWD = 1.5, n = 19, 1σ), and one xenocrystic zircon (~363 Ma) was found. Twenty-two zircon analysis spots from sample ZK2-19 (Figure 3c,d) yielded concordant results with a weighted mean $^{206}Pb/^{238}U$ age of 273.6 ± 2.6 Ma (Figure 4c; MSWD = 2.5, 1σ), and one xenocrystic zircon (~358 Ma) was found (Table 1).

The zircon Ti contents can be used to constrain the zircon crystallizing temperature (Watson, Wark, & Thomas, 2006). The zircon Ti contents of sample SY-09 and ZK2-19 are 4.61–54.22 ppm (avg. 17.95 ppm) and 10.18–116.59 ppm (avg. 31.98 ppm), respectively. Considering the relatively high zircon Ti content, and minor quartz content in these samples, the Ti-in-zircon thermometer which contains rutile and quartz is likely reliable (Ferry & Watson, 2007). The temperatures were calculated using Geo-fO_2 software (W. Li et al.,
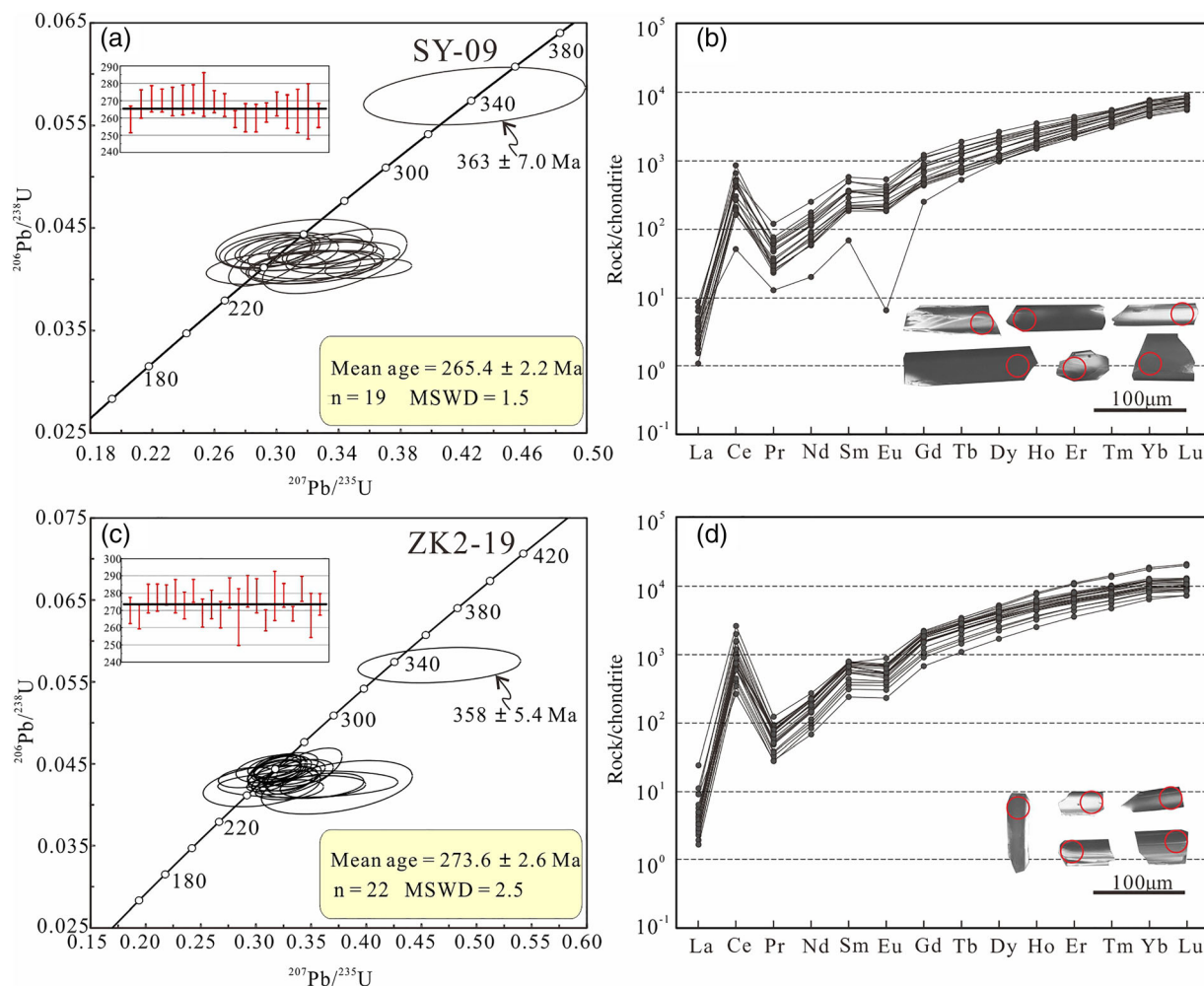
FIGURE 4 Concordia diagrams and chondrite-normalized REE patterns of zircon analyses for SY-09 (a,b) and Zk2-19 (c,d)

2019b) with assumed SiO_2 and TiO_2 activities of 1 (Ferry & Watson, 2007). The calculated temperatures for sample SY-09 and ZK2-19 are 678–935°C (avg. 795 °C) and 748–1,045°C (avg. 848°C), respectively (Table 2).

5.2 | Whole-rock geochemistry

The Shaquanzi hornblende gabbro samples have 45.31–50.17 wt% SiO_2, 0.88–1.99 wt% TiO_2, 14.30–18.30 wt% Al_2O_3, 6.97–11.19 wt% Fe_2O_3T, and 5.84–10.57 wt% MgO (Mg# = 63–70). They also have K_2O of 0.94–1.77 wt%, and Na_2O of 1.79–3.87 wt%, with total alkalis of 3.56–5.10 wt%, giving relatively consistent K_2O/Na_2O ratios (0.28–0.51, except one sample of 0.99). Their Cr (190.00–416.00 ppm) and Ni (93.14–162.00 ppm) contents are relatively high (Table 3). These samples plot in the sub-alkaline gabbro field in the TAS and SiO_2 vs. Nb/Y diagrams (Figure 5a,b). They are mainly medium- to high-K, and one sample falls in the shoshonite field (Figure 5c,d). In the chondrite-normalized REE variation patterns (Figure 6a; normalized to the chondrite values from Sun & McDonough, 1989), light-REEs (LREEs) are highly enriched relative to

heavy-REEs (HREEs) with $(La/Yb)_N$ = 3.27–7.86. Mid-REEs (MREEs) are weakly enriched relative to HREEs with $(Gd/Yb)_N$ = 1.83–2.66. They have moderately varying Eu anomalies (δEu = 0.94–1.03), suggesting no major plagioclase accumulation. In the primitive mantle-normalized multi-element variation diagrams (Figure 6b; normalized to the primitive mantle values from. Sun & McDonough, 1989), these samples show enrichment of LILEs (e.g., Rb, Ba, K, Pb and Sr) and depletion of HFSEs (e.g., Nb, Ta, Zr, Hf, and Ti). These geochemical features resemble the mafic intrusions at Tianyu and Baishiquan (Chai et al., 2008; Song et al., 2011; D. Tang et al., 2011) in the Central Tianshan Massif, but different from the mafic intrusions at Huangshan (incl. Huangshannan: Y. Zhao et al., 2015; Y. J. Mao et al., 2016; Huangshandong: Y. J. Mao et al., 2015; Huangshanxi: Mao, Qin et al., 2014; Huangshan: Deng et al., 2015) in the Kangguer ductile shear zone (Figure 6a,b).

5.3 | Whole-rock Sr–Nd–Pb isotopes

The Sr–Nd–Pb isotopic compositions of Shaquanzi hornblende gabbro are calculated on the base of 273.6 Ma for sample ZK2-19 and

TABLE 1 LA-ICP-MS zircon U–Pb isotopic analyses for Shaquanzi hornblende gabbro samples from the Shaquanzi area in the Aqishan–Yamansu Belt, eastern Tianshan

Sample no.	Th ppm	U ppm	Pb ppm	Th/U	Isotopic ratios						Ages (Ma)					
					$^{207}Pb/^{206}Pb$ Ratio	1δ	$^{207}Pb/^{235}U$ Ratio	1δ	$^{206}Pb/^{238}U$ Ratio	1δ	$^{207}Pb/^{206}Pb$ Ages	1δ	$^{207}Pb/^{235}U$ Ages	1δ	$^{206}Pb/^{238}U$ Ages	1δ
SY-09-1	597	319	22.9	1.8718	0.0518	0.0028	0.2933	0.0158	0.0410	0.0006	276	124	261	12.4	259	3.9
SY-09-2	1,349	594	49.2	2.2706	0.0528	0.0020	0.3109	0.0120	0.0425	0.0007	320	85.2	275	9.3	268	4.1
SY-09-3	755	326	26.6	2.3168	0.0550	0.0023	0.3255	0.0127	0.0429	0.0006	413	92.6	286	9.7	271	3.8
SY-09-4	1,211	537	42.8	2.2564	0.0500	0.0018	0.2984	0.0103	0.0428	0.0005	195	83.3	265	8.0	270	3.3
SY-09-5	1,318	576	46.7	2.2878	0.0524	0.0040	0.2959	0.0119	0.0427	0.0007	302	181	263	9.4	269	4.1
SY-09-6	41.6	112	8.10	0.3716	0.0525	0.0036	0.4278	0.0293	0.0579	0.0011	306	159.2375	362	20.8	363	7.0
SY-09-7	722	360	27.9	2.0051	0.0488	0.0025	0.2959	0.0133	0.0428	0.0007	139	119	263	10.4	270	4.3
SY-09-8	1,271	441	40.0	2.8859	0.0524	0.0028	0.3057	0.0121	0.0429	0.0007	302	122.2	271	9.4	271	4.1
SY-09-10	275	261	15.83	1.0529	0.0516	0.0035	0.3115	0.0207	0.0433	0.0010	333	157	275	16.0	274	6.3
SY-09-11	608	339	24.8	1.7916	0.0561	0.0026	0.3304	0.0143	0.0427	0.0005	454	102	290	10.9	269	3.1
SY-09-12	846	447	32.9	1.8921	0.0584	0.0028	0.3417	0.0155	0.0424	0.0005	543	108	298	11.8	267	3.3
SY-09-13	682	1,504	78.0	0.4539	0.0630	0.0020	0.3594	0.0115	0.0410	0.0004	709	68.5	312	8.6	259	2.4
SY-09-14	608	311	22.5	1.9560	0.0569	0.0030	0.3174	0.0151	0.0412	0.0007	487	114.8	280	11.7	260	4.1
SY-09-16	537	248	18.4	2.1609	0.0574	0.0031	0.3228	0.0167	0.0411	0.0006	506	119	284	12.8	260	4.0
SY-09-18	1832	719	58.9	2.5468	0.0590	0.0024	0.3377	0.0129	0.0417	0.0005	565	87.0	295	9.8	263	2.8
SY-09-19	2035	798	65.7	2.5504	0.0572	0.0020	0.3346	0.0115	0.0425	0.0006	498	75.9	293	8.8	268	3.4
SY-09-20	530	249	18.5	2.1243	0.0562	0.0031	0.3231	0.0190	0.0417	0.0008	461	129	284	14.6	264	4.8
SY-09-21	4,717	1,221	126	3.8625	0.0492	0.0022	0.2959	0.0109	0.0418	0.0010	167	102.8	263	8.6	264	6.2
SY-09-22	1,529	659	51.7	2.3209	0.0566	0.0032	0.3377	0.0191	0.0418	0.0013	476	124.1	295	14.5	264	8.0
SY-09-25	475	237	17.1	2.0059	0.0569	0.0030	0.3271	0.0170	0.0414	0.0006	487	117	287	13.0	262	3.4
ZK2-19-1	105	168	12.43	0.6244	0.0584	0.0034	0.4664	0.0302	0.0570	0.0009	546	160	389	20.9	358	5.4

Sample															
ZK2-19-4	1,027	637	44.6	1.6126	0.0546	0.0019	0.3237	0.0113	0.0428	0.0006	398	77.8	285	8.7	270	3.8
ZK2-19-5	590	272	21.1	2.1659	0.0605	0.0035	0.3516	0.0197	0.0422	0.0006	633	124	306	14.8	266	3.5
ZK2-19-6	6,846	1,221	158	5.6093	0.0559	0.0021	0.3402	0.0123	0.0439	0.0007	450	83.3	297	9.4	277	4.2
ZK2-19-7	850	416	33.8	2.0452	0.0553	0.0025	0.3316	0.0128	0.0440	0.0006	433	98.1	291	9.8	277	3.9
ZK2-19-9	22,718	2,798	438	8.1203	0.0521	0.0014	0.3197	0.0088	0.0442	0.0005	300	61.1	282	6.8	279	2.9
ZK2-19-10	1,109	509	40.5	2.1798	0.0519	0.0019	0.3196	0.0110	0.0441	0.0008	280	83.3	282	8.5	278	4.8
ZK2-19-11	1,427	643	51.9	2.2185	0.0528	0.0021	0.3245	0.0129	0.0432	0.0006	320	90.7	285	9.9	273	3.9
ZK2-19-12	2,105	987	78.8	2.1335	0.0509	0.0017	0.3170	0.0100	0.0446	0.0005	235	77.8	280	7.7	281	3.3
ZK2-19-13	1,647	812	66.7	2.0281	0.0486	0.0023	0.3474	0.0335	0.0425	0.0007	128	109	303	25.2	268	4.1
ZK2-19-14	8,256	2,177	221	3.7916	0.0547	0.0019	0.3333	0.0107	0.0433	0.0007	398	79.6	292	8.1	274	4.2
ZK2-19-16	1,189	536	43.0	2.2186	0.0603	0.0026	0.3600	0.0156	0.0424	0.0006	617	94	312	11.6	268	3.8
ZK2-19-17	1,039	521	39.8	1.9963	0.0509	0.0023	0.3162	0.0141	0.0444	0.0007	235	105.5	279	10.8	280	4.3
ZK2-19-19	1,403	703	49.1	1.9956	0.0681	0.0055	0.3735	0.0280	0.0421	0.0013	870	169.6	322	20.7	266	8.3
ZK2-19-20	2,010	973	84.8	2.0660	0.0487	0.0021	0.3271	0.0120	0.0446	0.0007	200	103.7	287	9.2	281	4.6
ZK2-19-21	3,943	1,028	115	3.8341	0.0522	0.0018	0.3185	0.0108	0.0441	0.0008	300	81.5	281	8.3	278	4.9
ZK2-19-22	660	430	30.3	1.5352	0.0570	0.0022	0.3305	0.0127	0.0418	0.0005	494	85.2	290	9.7	264	3.1
ZK2-19-23	1,658	841	67.4	1.9715	0.0564	0.0020	0.3438	0.0141	0.0441	0.0012	478	77.8	300	10.6	278	7.1
ZK2-19-24	2,145	755	71.2	2.8399	0.0518	0.0016	0.3185	0.0093	0.0442	0.0006	276	65.7	281	7.2	279	3.4
ZK2-19-25	7,029	2,298	206	3.0583	0.0524	0.0012	0.3084	0.0068	0.0425	0.0003	302	50.0	273	5.3	268	2.1
ZK2-19-27	1782	956	77.5	1.8639	0.0517	0.0015	0.3194	0.0088	0.0448	0.0006	272	66.7	281	6.8	283	3.6
ZK2-19-29	1,550	723	54.5	2.1420	0.0517	0.0029	0.3055	0.0218	0.0423	0.0010	333	97.2	271	16.9	267	6.4
ZK2-19-30	946	485	39.2	1.9512	0.0486	0.0018	0.2927	0.0109	0.0433	0.0005	128	88.9	261	8.6	274	3.1

TABLE 2 Zircon trace elements and Ti-in-zircon temperature for Shaquanzi hornblende gabbro samples from the Shaquanzi area in the Aqishan–Yamansu Belt, eastern Tianshan

| Sample no. | REEs (ppm) | | | | | | | | | | | | | | Ti (ppm) | T (°C) |
	La	Ce	Pr	Nd	Sm	Eu	Gd	Tb	Dy	Ho	Er	Tm	Yb	Lu		
SY-09-1	0.26	124	2.19	28.1	30.4	11.0	101	29.4	309	107	470	105	1,051	210	15.9	792
SY-09-2	0.77	318	4.53	52.6	53.6	17.1	177	50.8	513	162	630	133	1,263	210	13.1	772
SY-09-3	0.90	183	5.98	67.7	55.1	22.1	144	38.2	381	123	508	113	1,123	205	18.0	805
SY-09-4	1.07	248	5.58	59.8	52.0	19.7	165	46.1	470	152	617	134	1,289	226	12.0	764
SY-09-5	1.18	258	5.74	62.8	54.1	20.3	169	45.5	449	138	536	111	1,050	180	10.86	754
SY-09-6	0.57	6.69	0.17	1.06	0.88	0.20	5.76	2.30	33.0	14.7	78	19.1	202	46.2	4.61	678
SY-09-7	0.93	159	4.44	51.5	43.5	17.8	135	37.6	378	121	491	103	988	175	20.7	820
SY-09-8	2.05	311	11.2	115	87.0	30.5	230	58.4	547	161	619	129	1,201	208	21.3	823
SY-09-10	11.81	42.9	3.06	17.0	7.46	1.20	30.6	10.62	137	54.0	249	55.6	553	102.5	11.40	759
SY-09-11	0.49	126	2.45	26.7	27.8	10.5	94.1	27.0	289	96.6	405	88.4	888	157	15.0	786
SY-09-12	0.59	164	2.83	31.7	31.5	12.1	102	30.0	309	102	425	93.5	898	160	28.7	856
SY-09-13	1.00	30.9	1.22	9.33	10.4	0.38	50.9	19.4	244	90.6	400	82.9	748	137	15.37	788
SY-09-14	0.50	116	2.91	33.6	29.5	12.7	88.0	24.7	254	85.8	382	87.7	906	174	14.1	779
SY-09-16	0.51	118	3.52	41.5	33.6	13.3	102.8	27.1	275	92.9	382	84.9	826	155	19.1	811
SY-09-18	1.73	396	7.14	81.0	74.7	23.0	221	59.1	567	170	662	137	1,271	222	15.9	792
SY-09-19	0.64	300	2.33	27.3	31.0	10.7	115	35.5	377	129	541	114	1,083	202	16.3	794
SY-09-20	0.43	113	3.27	41.1	36.5	15.3	108	29.7	296	98.5	423	93.5	938	178	23.1	832
SY-09-21	1.50	516	6.35	72.1	74.8	24.8	247	69.9	661	196	715	139	1,220	197	54.2	935
SY-09-22	0.90	302	4.83	53.8	53.4	17.6	181	50.5	498	153	580	119	1,090	184	11.7	761
SY-09-25	0.36	97.4	2.76	35.8	32.9	12.5	92.7	25.4	250	84.0	352	78.2	777	145	17.6	803
ZK2-19-1	0.0077	14.4	0.033	1.09	2.65	1.38	19.0	8.37	130	59.7	320	79.8	865	185	10.2	748
ZK2-19-4	0.63	387	4.54	64.9	80.9	27.5	311	86.4	865	272	1,024	191	1,587	247	46.9	916
ZK2-19-5	2.15	159	2.67	31.1	36.0	13.2	137	40.1	424	140	580	118	1,070	183	17.8	803
ZK2-19-6	2.12	1,201	8.44	101.9	100.0	31.0	356	93.3	924	295	1,133	227	1,988	318	51.5	928
ZK2-19-7	0.53	241	3.07	42.4	53.7	20.1	204	58.8	615	199	795	157	1,372	220	116.6	1,045
ZK2-19-9	5.62	1,574	11.5	124	115	50.3	449	126	1,305	446	1,797	355	3,100	520	37.6	888
ZK2-19-10	0.81	364	7.29	96.4	107	37.9	354	94.3	909	272	1,005	189	1,592	238	14.4	782
ZK2-19-11	0.45	369	3.60	51.6	65.6	23.2	255	72.9	763	244	945	185	1,577	243	11.7	762
ZK2-19-12	0.74	454	4.89	68.6	83.5	29.8	310	84.3	841	256	956	178	1,438	218	31.6	867
ZK2-19-13	0.59	424	5.12	71.3	88.7	30.3	321	87.0	873	266	983	184	1,532	225	28.8	856
ZK2-19-14	2.59	926	8.68	101	102	40.6	414	116	1,248	425	1,731	338	2,942	497	33.6	875
ZK2-19-16	1.11	432	8.13	105	117	40.9	391	103	982	292	1,061	200	1,680	256	20.6	819

Sample																
ZK2-19-17	0.67	357	5.54	75.5	88.9	31.0	314	85.1	822	252	915	174	1,467	219	13.7	777
ZK2-19-19	1.01	484	6.95	98	112	39.4	402	109	1,083	331	1,226	234	1,964	300	52.5	930
ZK2-19-20	0.98	652	6.32	85.1	101	30.8	374	103	1,031	310	1,137	216	1,790	270	19.1	811
ZK2-19-21	1.33	719	7.56	104	115	37.5	401	107	1,043	314	1,164	220	1,856	282	27.3	850
ZK2-19-22	0.39	206	2.60	38.2	46.6	17.3	183	53.1	557	180	704	138	1,162	182	12.4	767
ZK2-19-23	0.90	520	7.13	96.0	114	39.0	404	110	1,105	334	1,254	238	1,952	282	14.1	780
ZK2-19-24	1.14	596	7.36	102	119	41.1	434	120	1,177	360	1,347	254	2,134	322	15.1	786
ZK2-19-25	1.17	946	6.26	86.8	99.3	31.3	369	102	1,018	330	1,269	242	1,996	323	47.1	916
ZK2-19-27	1.16	538	6.38	82.8	100	35.6	374	105	1,060	340	1,301	247	2,035	309	20.1	817
ZK2-19-29	0.77	448	4.72	66.9	81.4	25.8	304	84.2	856	273	1,054	198	1,621	264	19.2	811
ZK2-19-30	1.49	268	3.46	46.7	58.5	22.2	216	62.9	641	206	801	154	1,340	210	73.7	977

ZK2-119, and 265.4 Ma for sample SY-09. All samples have relatively low $^{87}Sr/^{86}Sr$ ratios of 0.704946–0.705386 and $^{143}Nd/^{144}Nd$ ratios of 0.512674–0.512762, with narrow initial Sr isotope (($^{87}Sr/^{86}Sr)_i$) range (0.7047–0.7049) and positive $\varepsilon_{Nd}(t)$ values (3.34–4.44) (Table S1). The corresponding single-stage depleted mantle Nd model ages (T_{DM1}) range from 1,000 to 773 Ma (avg. 853 Ma). They have restricted $^{206}Pb/^{204}Pb$ (18.19–18.30) and ($^{206}Pb/^{204}Pb)_i$ (17.85 to 17.97) values (Table S1). In the $\varepsilon_{Nd}(t)$ vs. ($^{87}Sr/^{86}Sr)_i$ diagram (Figure 7a), these samples scatter in the field of the Late Carboniferous igneous rocks in the Aqishan–Yamansu Belt, which had been interpreted to be derived from juvenile crust source with minor mantle input or a depleted mantle source (Du et al., 2018; Jiang et al., 2017; Zhang et al., 2016, W. Zhang et al., 2017; S. Zhang, Chen, Hollings, Zhao, & Gong, 2020; Zhao et al., 2018a, L. Zhao et al., 2019b). They also plot near the fields of Permian granites and Early Carboniferous igneous rocks, which had been interpreted to form from partial melting of Mesoproterozoic lower crust or juvenile crust with some mantle-derived input, or mantle source with ancient crust contamination (Du et al., 2018; B. Wu, 2019; D. Y. Zhang, 2012; S. Zhang et al., 2020; L. Zhao et al., 2019a). Compared to mafic-ultramafic intrusions in the Kangguer ductile shear zone, the Shaquanzi hornblende gabbro has lower $\varepsilon_{Nd}(t)$ and higher ($^{87}Sr/^{86}Sr)_i$, but similar to those of mafic-ultramafic intrusions in the Central Tianshan Massif. In the ($^{87}Sr/^{86}Sr)_i$ vs. ($^{206}Pb/^{204}Pb)_i$ diagram (Figure 7b), our samples plot in the overlapping field between MORB and OIB, and also close to mafic-ultramafic intrusions in the Central Tianshan Massif, displaying an evolution trend toward EMI.

5.4 | In situ zircon Hf isotopes

Ten dated zircons from sample SY-09 yielded $^{176}Lu/^{177}Hf = 0.001021$–0.005426 and $^{176}Hf/^{177}Hf = 0.282712$–0.282889. When calculated with the crystallization age of each zircon grain, the $\varepsilon_{Hf}(t)$ values mainly vary between $+2.8$ and $+8.7$, whereas the xenocrystic zircon has high $\varepsilon_{Hf}(t)$ (11.9). They all plot in the field of East CAOB (Figure 8a). The $\varepsilon_{Hf}(t)$ values of the Shaquanzi hornlende gabbro lie in the field of the Central Tianshan mafic intrusions, but lower than those from the Kangguer ductile shear zone (Figure 8b,c; Table S2). The corresponding $T_{DM} = 865$–515 Ma (avg. 691 Ma) are older than those from the Kangguer ductile shear zone but close to those from the Central Tianshan Massif (Figure 8d).

6 | DISCUSSION

6.1 | Age of the Shaquanzi hornblende gabbro

Previous geochronological studies on the Shaquanzi Fe–Cu deposit were mainly dedicated to the mineralization, ore-hosting volcanic rocks, and intermediate-felsic intrusive rocks there (Jiang et al., 2017, 2018). However, little attention has been paid to the mafic-ultramafic intrusions. The Shaquanzi hornblende gabbro shows intrusive

TABLE 3 The whole-rock major (wt%) and trace elements (ppm) of Shaquanzi hornblende gabbro samples from the Shaqanzi area in the Aqishan–Yamansu Belt, eastern Tianshan

Sample. No.	SY-09	S14-009	S14-010	S14-010+	ZK2-10	ZK2-19	ZK1-119
Rock type	Coarse-grained	Coarse-grained	Coarse-grained	Coarse-grained	Medium-grained	Medium-grained	Medium-grained
Major elements (wt%)							
SiO_2	48.51	49.20	47.80	48.50	45.31	47.02	50.17
TiO_2	1.12	1.10	1.26	1.18	0.88	1.99	1.12
Al_2O_3	17.65	18.30	18.05	17.65	14.30	14.54	16.51
Fe_2O_3T	7.22	7.89	6.97	7.51	11.19	10.73	9.17
MnO	0.12	0.14	0.14	0.15	0.24	0.17	0.15
MgO	6.44	6.40	5.84	7.56	10.57	8.41	6.60
CaO	9.39	10.05	9.66	9.03	8.72	8.68	8.19
Na_2O	3.87	3.44	3.78	3.13	1.79	3.57	3.35
K_2O	1.23	1.18	1.22	1.59	1.77	1.32	0.94
P_2O_5	0.29	0.26	0.38	0.32	0.19	0.58	0.32
LOI	3.02	1.96	3.30	2.64	3.27	2.28	3.01
Total	98.86	99.92	98.40	99.26	98.23	99.29	99.53
Trace elements (ppm)							
Li	16.00	13.87	24.84	26.59	16.20	11.90	19.60
Be	0.93	1.15	1.09	1.28	0.54	1.67	1.02
Sc	26.10	28.82	28.27	30.88	35.70	27.50	23.70
V	143.00	180.94	179.83	175.21	266.00	209.00	219.00
Cr	276.00	334.58	364.52	371.15	416.00	247.00	190.00
Co	29.80	33.93	28.03	35.48	45.10	36.30	31.20
Ni	105.00	105.53	93.14	120.12	162.00	131.00	95.70
Cu	72.10	72.77	84.81	99.12	55.80	44.30	54.30
Zn	67.00	139.72	128.06	120.85	129.00	98.00	77.00
Ga	18.50	17.21	17.14	16.42	17.55	18.95	19.05
Rb	16.40	28.34	49.18	52.41	41.30	25.30	14.20
Sr	707.00	639.37	606.74	541.09	270.00	554.00	681.00
Y	18.20	18.35	22.08	19.36	17.00	33.80	19.50
Zr	110.50	127.29	189.02	167.89	61.90	186.50	100.50
Nb	4.10	3.75	5.14	4.15	1.80	10.80	4.10
Cs	1.32	4.94	1.16	2.79	1.16	0.58	0.50
Ba	250.00	214.98	198.49	281.56	350.00	410.00	190.00
La	13.20	12.01	17.85	14.66	7.80	29.20	12.30
Ce	33.30	29.83	48.05	39.59	19.50	78.30	30.70
Pr	4.47	4.05	6.71	5.61	2.91	11.55	4.14
Nd	19.70	17.40	30.09	25.06	12.90	46.30	18.50
Sm	4.47	3.70	6.12	5.29	3.41	9.30	4.66
Eu	1.42	1.21	1.79	1.59	1.14	2.79	1.47
Gd	4.10	3.46	5.23	4.53	3.79	8.79	4.61
Tb	0.61	0.54	0.77	0.66	0.58	1.26	0.70
Dy	3.60	3.08	3.99	3.52	3.41	7.05	4.06
Ho	0.72	0.60	0.72	0.66	0.69	1.39	0.81
Er	2.03	1.73	1.96	1.81	1.89	3.67	2.22
Tm	0.27	0.23	0.26	0.24	0.25	0.48	0.29
Yb	1.77	1.41	1.63	1.42	1.71	3.00	1.95

TABLE 3 (Continued)

Sample. No.	SY-09	S14-009	S14-010	S14-010+	ZK2-10	ZK2-19	ZK1-119
Rock type	Coarse-grained	Coarse-grained	Coarse-grained	Coarse-grained	Medium-grained	Medium-grained	Medium-grained
Lu	0.27	0.21	0.23	0.20	0.25	0.43	0.29
Hf	2.90	2.69	3.93	3.49	1.90	4.70	3.00
Ta	0.27	0.37	0.35	0.26	0.10	0.55	0.26
W	0.20	0.47	0.64	0.38	0.50	0.40	0.20
Tl	0.17	0.11	0.15	0.20	0.24	0.11	0.12
Pb	6.20	4.97	7.07	8.18	2.20	3.60	6.20
Bi	0.02	0.09	0.07	0.07	0.04	0.01	0.01
Th	1.00	1.03	1.39	1.08	1.30	1.60	1.40
U	0.80	0.57	0.57	0.47	0.50	0.50	0.60
Ti	6,713.27	6,593.39	7,552.43	7,072.91	5,274.71	11,928.04	6,713.27
Mg#	68	65	66	70	69	65	63
REE	89.93	79.45	125.41	104.85	60.23	203.51	86.70
$(La/Yb)_N$	5.35	6.13	7.86	7.40	3.27	6.98	4.52
$(La/Sm)_N$	1.91	2.10	1.88	1.79	1.48	2.03	1.70
$(Gd/Yb)_N$	1.92	2.03	2.66	2.63	1.83	2.42	1.96
δEu	1.01	1.03	0.97	0.99	0.97	0.94	0.97
$Na_2O + K_2O$	5.10	4.62	5.00	4.72	3.56	4.89	4.29
K_2O/Na_2O	0.32	0.34	0.32	0.51	0.99	0.37	0.28

Note: Mg# = molar Mg/(Mg + Fe); δEu = Eu_N/SQRT(Sm_N*Gd_N); Normalized to the chondrite values from Sun and McDonough (1989).

relations with the Upper Carboniferous (ca. 328–303 Ma; Jiang et al., 2017; F. Liu et al., 2019) Shaquanzi Formation volcanic sequence (Figure 2). Our new Permian zircon U–Pb ages on the Shaquanzi hornblende gabbro (265.4 ± 2.2 Ma and 273.6 ± 2.6 Ma) are clearly younger than the Shaquanzi Formation, but broadly coeval to the eastern Tianshan mafic-ultramafic intrusions (Figure 9; Table S3). Combined with the published geochronological data of the mafic-ultramafic intrusions from the neighbouring region (e.g., Kangguer ductile shear zone and Central Tianshan Massif), we suggested that the Permian mafic magmatism also occurred in the Aqishan–Yamansu Belt.

6.2 | Petrogenesis of the Shaquanzi hornblende gabbro

6.2.1 | Alteration and crustal contamination

The Shaquanzi hornblende gabbro has relatively high LOI (1.96–3.30 wt%), implying that they may have undergone certain degree of post-magmatic alteration, as also indicated by petrographic observations (chlorite/sericite alteration). This alteration may have been resulted from low-grade metamorphism or fluid–rock interactions. Previous studies suggested that elements including Al, Ti, P, HFSEs, REEs (except Ce and Eu), and transition metals are typically immobile,

whereas Ca, Na, and LILEs are readily mobilized by alteration (Polat & Hofmann, 2003; Yan et al., 2015). Our samples exhibit relatively constant Na_2O (1.89–4.04 wt%) and K_2O (0.97–1.96 wt%) contents with narrow K_2O/Na_2O range (0.28–0.99), and the elements of Na_2O and K_2O display scattered trends with LOI (Figure 10a,b), suggesting the major elements remained largely immobile. Moreover, Rb displays no correlation with LOI (Figure 10c), and the ranges of Rb (14.2–52.41 ppm), Ba (190–410 ppm), and Ba/Rb (4.04–16.21) are all narrow. Both Rb and Ba show positive correlation with K_2O (Figure 10d), implying that the LILEs are also likely immobile in our samples. All these suggest that the alteration effect on the whole-rock geochemical compositions is very limited.

Mantle-derived magmas commonly ascend through the continental crust and evolve inside crustal-level magma chambers, indicating that crust contamination is inevitable (Watson, 1982; Yan et al., 2015). The presence of Late Devonian xenocrystic zircons (ca. 363 and 358 Ma) from sample SY-09 and ZK2-19 implies crustal contamination in the gabbroic magma. Crustal components generally contain high SiO_2 and $^{87}Sr/^{86}Sr$ ratios, but distinctly low $ε_{Nd}$(t) and MgO content, and thus any crustal contamination would cause a $(^{87}Sr/^{86}Sr)_i$ rise and a $ε_{Nd}$(t) drop to the magma (Rogers et al., 2000; Rudnick and Fountain, 1995). However, the Shaquanzi hornblende gabbro samples have similarly positive $ε_{Nd}$(t) (3.34–4.44) values and low $(^{87}Sr/^{86}Sr)_i$ (0.7047–0.7049), which argues against significant crustal contamination. In addition, mafic magma contaminated by
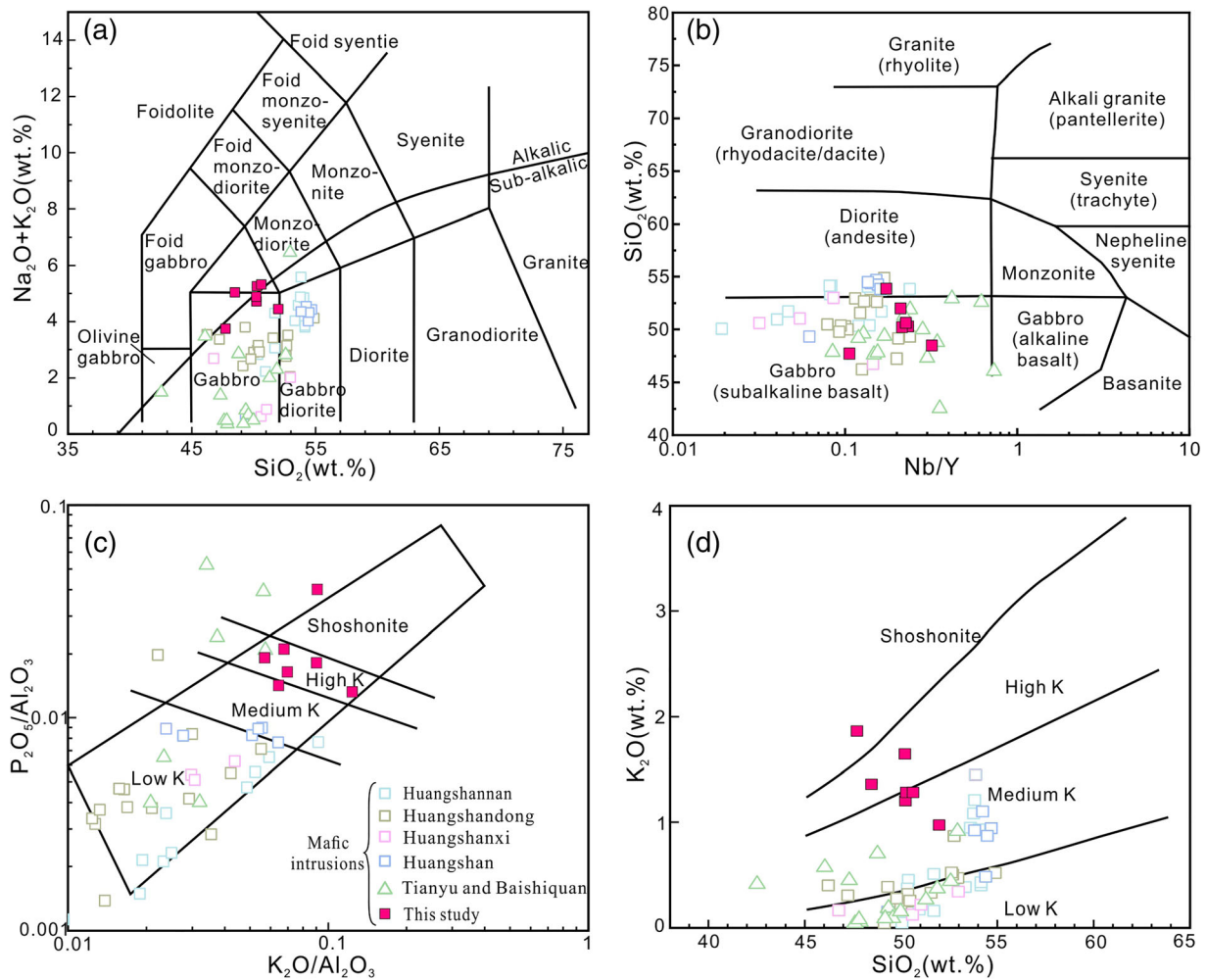
FIGURE 5 (a) Total alkali-silica (TAS) diagram (after Middlemost, 1994); (b) SiO$_2$ vs. Nb/Y diagram (after Winchester and Floyd, 1977); (c) P$_2$O$_5$/Al$_2$O$_3$ vs. K$_2$O/Al$_2$O$_3$ diagram (after Crawford, Meffre, Squire, Barron, & Falloon, 2007). (d) SiO$_2$ vs. K$_2$O compositions of the Shaquanzi hornblende gabbro samples (after Peccerillo & Taylor, 1976). Data source: Tianyu and Baishiquan (Chai et al., 2008; Song et al., 2011; D. Tang et al., 2011); Huangshannan (Y. J. Mao et al., 2016; Y. Zhao et al., 2015), Huangshandong (Y. J. Mao et al., 2015), Huangshanxi (Mao et al., 2014), Huangshan (Deng et al., 2015)
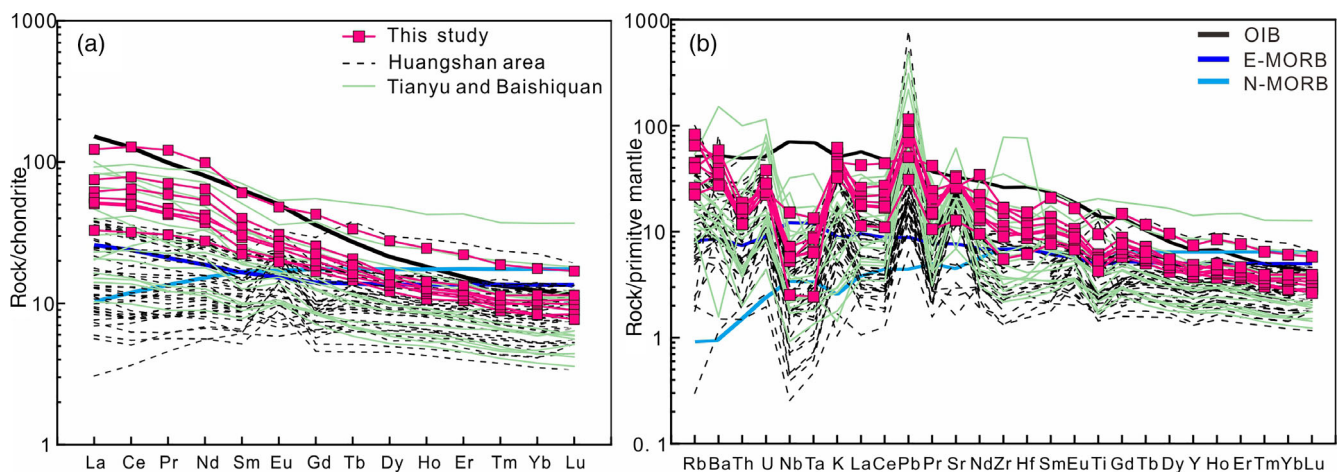
FIGURE 6 Chondrite-normalized REE patterns (a) and primitive mantle-normalized trace element variation diagrams (b) of the Shaquanzi hornblende gabbro samples. Normalizing values, OIB, E-MORB and N-MORB are from. Sun and McDonough (1989). Data source are as in Figure 5. Huangshan data include those from Huangshannan, Huangshandong, Huangshanxi, and Huangshan
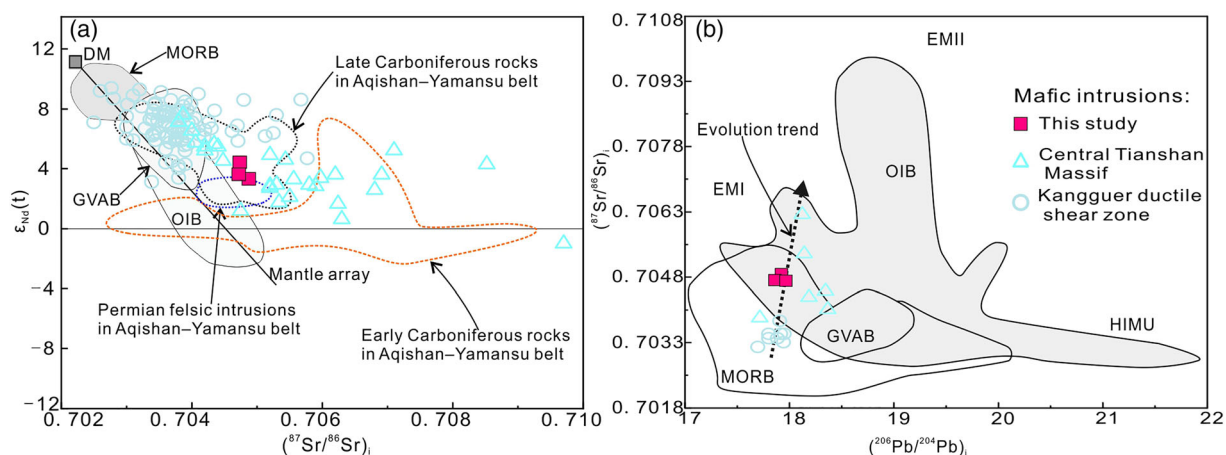
FIGURE 7 (a) Initial $\varepsilon_{Nd}(t)$ vs. $(^{87}Sr/^{86}Sr)_i$ diagram; (b) $(^{87}Sr/^{86}Sr)_i$ vs. $(^{206}Pb/^{204}Pb)_i$ diagram after Zindler and Hart (1986). GVAB, global volcanic arc basalts. Sr–Nd–Pb isotope data source: Central Tianshan Massif (Chai et al., 2008; Song et al., 2011; D. Tang et al., 2011); Kangguer ductile shear zone (Deng et al., 2015; Gao et al., 2013; Y. J. Mao et al., 2016; T. Sun, Qian, Deng, et al., 2013a; T. Sun, Qian, Li, et al., 2013b; D. Tang et al., 2013; Xia et al., 2008; M. F. Zhou et al., 2004)
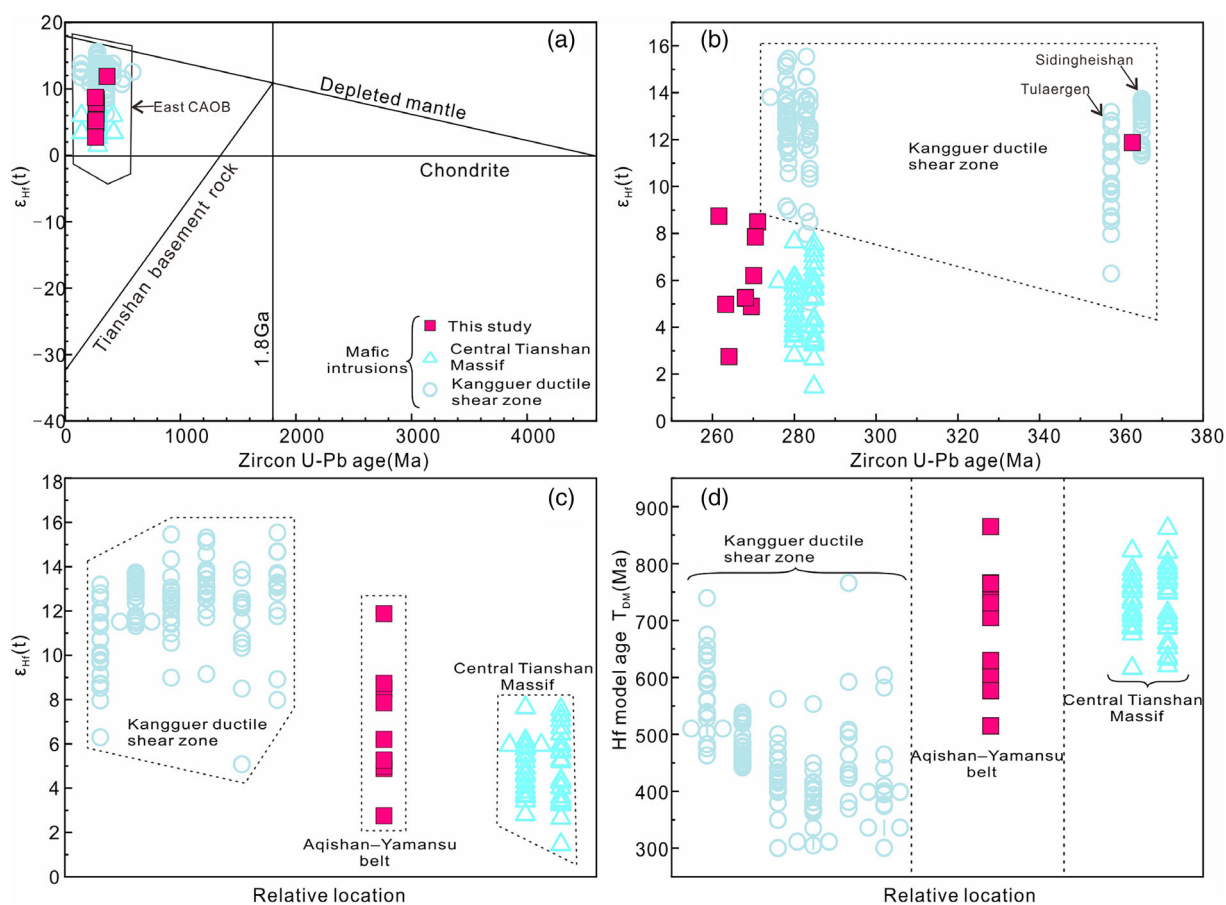
FIGURE 8 Relationship between $\varepsilon_{Hf}(t)$ and U–Pb age for zircons from the Shaquanzi hornblende gabbro and the eastern Tianshan mafic-ultramafic complexes (a,b); Zircon $\varepsilon_{Hf}(t)$ and Hf model ages of the mafic-ultramafic intrusions in the eastern Tianshan (c,d) . East CAOB (Qian et al., 2014); Central Tianshan Massif (Su et al., 2011); Kangguer ductile shear zone (Y. J. Mao et al., 2016; Qin et al., 2011; San et al., 2010; Shi et al., 2018; Su et al., 2011; T. Sun, Qian, Li, et al., 2013b)

crustal materials would lead to increasing La/Nb and the decreasing Ce/Pb (W. Sun et al., 2008; Yan et al., 2015), which are not found in our samples (Figure 10e,f). Meanwhile, the isotopic/trace elemental

ratios (e.g., $(^{87}Sr/^{86}Sr)_i$, $\varepsilon_{Nd}(t)$, Nb/La), which are sensitive to crustal contamination, do not show any correlation with MgO content (Figure 10g,h; Jiang et al., 2017; H. Wang et al., 2013). Taken

together, the chemical and isotopic data suggest that crustal contamination for the Shaquanzi hornblende gabbro was insignificant.

6.2.2 | Fractional crystallization

Previous studies indicate that mantle-derived primary magmas have high Ni (>400 ppm), Cr (>1,000 ppm), and Mg# (73–81) (e.g., Wilson, 1989). The Shaquanzi hornblende gabbro has relatively low Mg# (63–70) and varying Cr (190–416 ppm) and Ni (93–162 ppm) contents. The samples define clear fractionation trend in the Ce/Sm vs. Sm plot and negative SiO_2 vs. MgO correlation, suggesting the occurrence of fractional crystallization (Figure 11a,b; Allègre & Minster, 1978; Schiano, Monzier, Eissen, Martin, & Koga, 2010). The positive correlations between Cr, Ni, and MgO (Figure 11c,d) suggest the fractionation of olivine and/or pyroxenes. However, the positive Fe_2O_3T–MgO trend and the lack of CaO vs. MgO correlation suggest that olivine fractionation likely predominated (Figure 12a,b), which is supported by the absence of olivine in these studied rocks. The lack of TiO_2 vs. MgO correlation implies insignificant fractionation of Fe–Ti oxides in the magma (Figure 12c), while the positive K_2O vs. MgO correlation likely reflects hornblende fractionation (Figure 12d). With decreasing MgO contents, the relatively consistent CaO and increasing in Al_2O_3 and Sr contents, together with the slight Eu anomalies imply that plagioclase was not a major fractionation product (Figure 12b,e,f). Thus, the

parental magma of Shaquanzi intrusion may have mainly undergone olivine-dominated fractionation and minor hornblende fractionation.

6.2.3 | Nature of mantle source

The Shaquanzi hornblende gabbro samples display zircon $^{176}Hf/^{177}Hf$ ratios of 0.282712–0.282889 with relatively high positive $\varepsilon_{Hf}(t)$ values (2.8–8.7), indicating a depleted mantle source. Moreover, they have low $(^{87}Sr/^{86}Sr)_i$ (0.7047–0.7049) and positive $\varepsilon_{Nd}(t)$ values (3.34–4.44), accord with their possible formation from a depleted mantle source. However, the relatively wide zircon $\varepsilon_{Hf}(t)$ range and the old T_{DM} (515–865 Ma) suggest that the depleted mantle source was subjected to certain enrichment processes (Su et al., 2011).

Our samples display LREEs and LILEs enrichments but HFSEs depletions (Figure 6a,b). This feature can result from crustal contamination or subduction-related process (Jiang et al., 2017). However, rocks formed by crustal contamination should also have positive Zr–Hf anomalies owing to the enrichments of them in crustal materials (H. Wang et al., 2013). The Zr–Hf depletions in the Shaquanzi gabbroic rocks imply that crustal contamination is minor, which is also supported by other chemical and isotopic data above-mentioned. Moreover, the Th/Yb vs. Nb/Yb and Nb/U vs. Nb diagrams are often used to illustrate crustal contamination vs. subduction-related inputs into the magmas (Chung et al., 2001; Deng et al., 2015; Jiang et al., 2017; Pearce, 2008). Almost all our samples fall above the mantle array, plotting in the volcanic arc basalt (VAB) field (Figure 13a), and have lower Nb/U ratios than the upper crust (Figure 13b), which indicate that subduction-related input likely predominates. The decoupling of trace element vs. isotope features of these samples indicates that the depleted mantle source had suffered previous modification before generating the Shaquanzi gabbroic magma. The Shaquanzi samples have varying but generally high Ba/La ratios (11.1–44.9) and pronounced LILE enrichments, suggesting that the metasomatic agent was probably slab-derived fluids (Figure 13c; Woodhead et al., 2001). Furthermore, the rocks have consistently low Th contents (1.00–1.60 ppm) and higher Ba/Th ratios (135.7–269.2), which also suggest that they were modified by slab-derived fluids (Figure 13d; Pearce, Stern, Bloomer, & Fryer, 2005). This conclusion is consistent with their hydrous mineral assemblage, which includes abundant hornblende (Zhao & Zhou, 2007).

The degree of partial melting and source mineralogy of the mantle source can be modelled using the REE abundance and ratios (Aldanmaz et al., 2000; J. H. Zhao & Zhou, 2009). Garnet often has high Yb content due to its high HREE partition coefficient, whereas the La and Sm contents are not significantly changed by variations in the source mineralogy (e.g., garnet or spinel; Y. Sun et al., 2019). Thus, mafic magmas generated by a spinel-bearing peridotite source would have lower Dy/Yb than those derived from a garnet-bearing peridotite source (Jung et al., 2006; Long et al., 2020), and increasing amount of garnet in the magma source residue would produce melts with decreasing Yb, but increasing Sm/Yb ratios. Partial melting of a spinel-lherzolite mantle source does not alter the Sm/Yb ratio due to

FIGURE 9 Mafic-ultramafic magmatic age histogram of the Palaeozoic eastern Tianshan Orogen (data source: J. P. Chen et al., 2016; B. Y. Chen et al. 2018 Deng et al., 2020; Feng et al., 2018; C. Han et al., 2010, 2013b; B. F. Han, Ji, Song, Chen, & Li, 2004; J. Y. Li et al., 2006; Y. J. Mao et al., 2016; Qin et al., 2011; San et al., 2010; Shi et al., 2018; Su et al., 2011, 2014; Y. Sun et al., 2019; T. Sun, Qian, Li, et al., 2013b; D. M. Tang et al., 2009, 2011; Y. W. Wang, Wang, Wang, & Long, 2009; H. Wu et al., 2005; Xia et al., 2008; Y. Zhao et al., 2015; Zhao et al., 2018a; M. F. Zhou et al., 2004; G. C. Zhou et al., 2019)
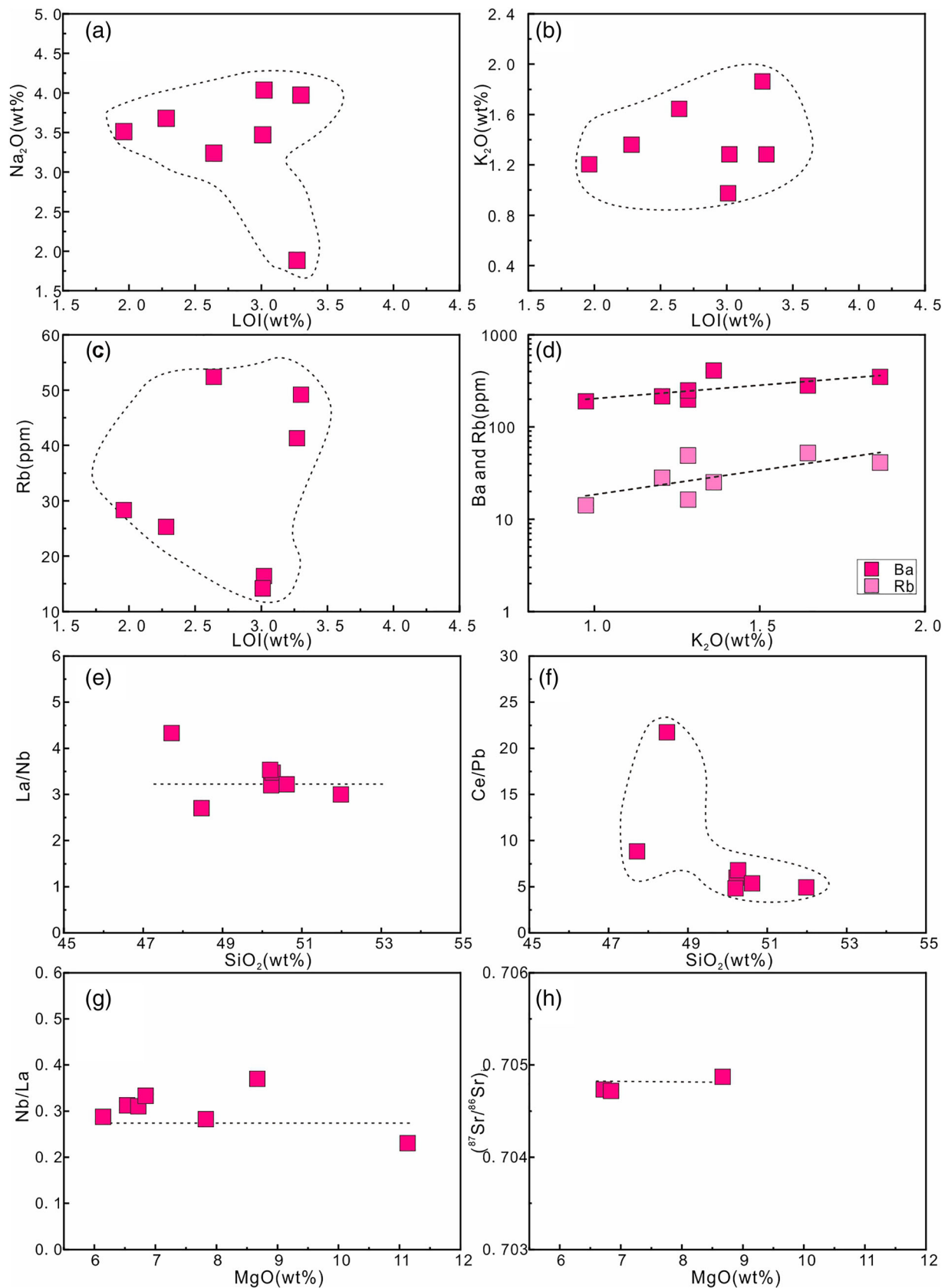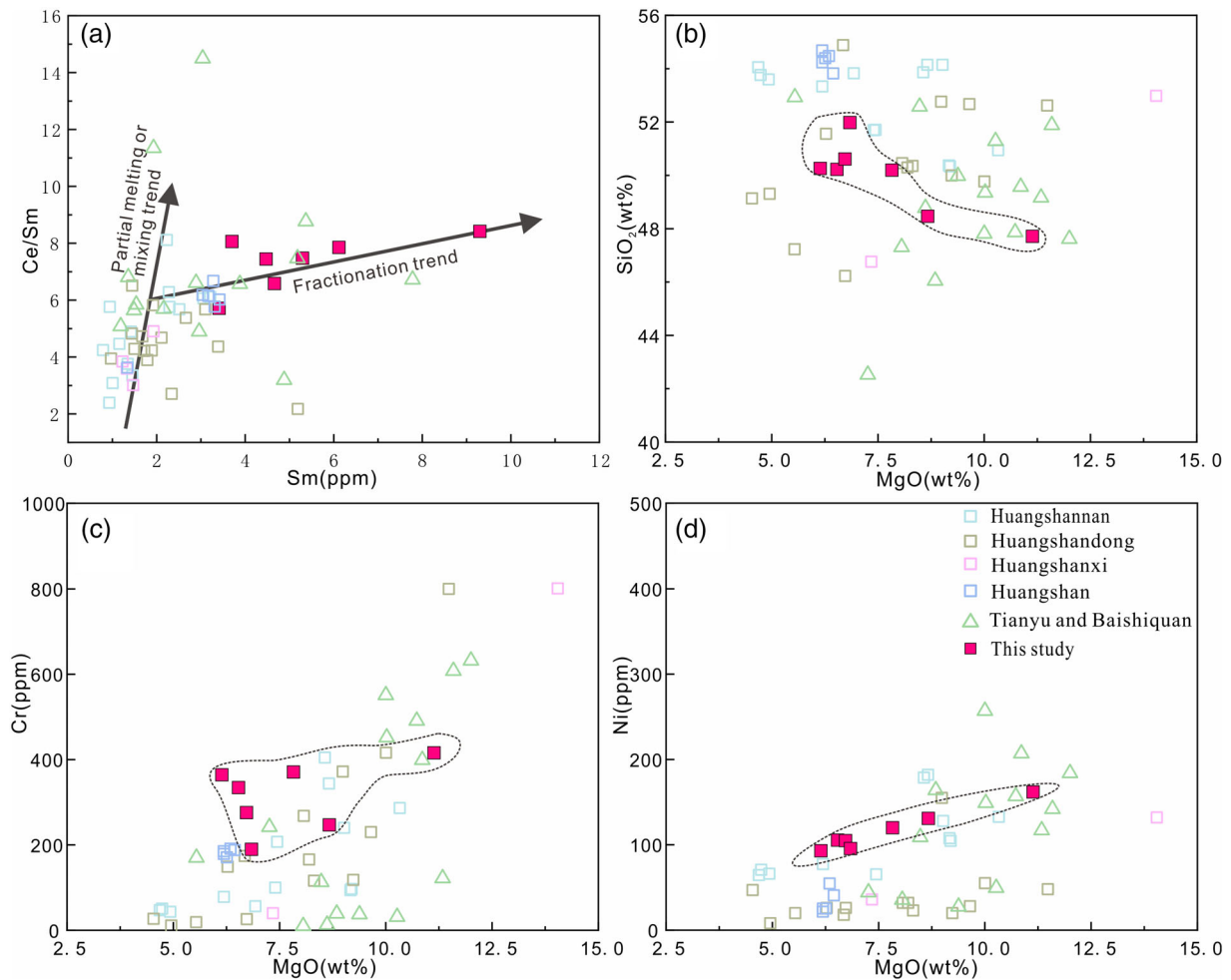
FIGURE 10 (a) Na$_2$O, (b) K$_2$O and (c) Rb vs. LOI diagrams; (d) Rb and Ba vs. K$_2$O diagram; (e) La/Nb and (f) Ce/Pb vs. SiO$_2$ diagrams; (g) Nb/La and (h) (^{87}Sr/^{86}Sr)$_i$ vs. MgO diagrams

FIGURE 11 (a) Ce/Sm, vs. Sm; (b) SiO₂, (c) Cr, and (d) Ni vs. MgO diagrams

the similar partition coefficients of Sm and Yb in spinel, and should define a melting trend along or sub-parallel to the mantle array (Aldanmaz et al., 2000; Zhao & Zhou, 2007). The Shaquanzi hornblende gabbro and many Central Tianshan mafic intrusions (e.g., Tianyu and Baishiquan) display higher Dy/Yb values than those from the Huangshan intrusions in the Kangguer ductile shear zone, and plot above or on the spinel-lherzolite melting curve (Figure 13e). Furthermore, the samples from Shaquanzi, Tianyu, and Baishiquan plot above the garnet-lherzolite melting trend, whereas data from the Huangshan intrusion display sub-parallel trend with the mantle array in the Sm/Yb vs. La/Sm diagram (Figure 13f). This indicates that the Shaquanzi hornblende gabbro and the Tianyu and Baishiquan mafic intrusions were likely generated with 10–30% partial melting of mantle source at a deeper depth (>85 km), corresponding to the garnet to garnet-spinel stability field (Herzberg, 1995; Robinson & Wood, 1998). In contrast, the mafic-ultramafic magma generation for the Huangshan intrusion may have occurred at a shallower depth (spinel stability field). Thus, the decreasing $\varepsilon_{Hf}(t)$ and $\varepsilon_{Nd}(t)$ values, and the increasing T_{DM} and $(^{87}Sr/^{86}Sr)_i$ of the mafic intrusions from the Kangguer ductile shear zone to the Aqishan-Yamansu belt and Central Tianshan Massif may have induced by the heterogeneous mantle source (Figures 7 and 8).

6.3 | Tectonic setting of the Shaquanzi mafic plutonism

As above-mentioned, our Permian Shaquanzi hornblende gabbro samples are sub-alkaline with arc-like geochemical features. However, magmas with arc-like geochemical characteristics can also be formed in non-arc setting, if the mantle source was metasomatized by subduction-related materials (Keppler, 1996; Y. Sun et al., 2019). Alaskan-type complexes generally contain a specific lithologic assemblage of dunite, wehrlite, olivine/hornblende clinopyroxenite, hornblendite, and hornblende gabbro (Irvine, 1974; Su et al., 2014), and their ultramafic rocks have rare orthopyroxene or plagioclase. The only mafic-ultramafic rock type identified at Shaquanzi is hornblende gabbro, together with other contemporary mafic-ultramafic intrusions in the eastern Tianshan (e.g., Xiangshan and Huangshannan) containing high abundance of orthopyroxene, suggest that these intrusions cannot be Alaskan-type.

Moreover, the discovery of post-collisional Early Permian A₂-type granites and the rarity of the latest Carboniferous volcanic and intrusive rocks (ca. 300 Ma; Du et al., 2018; S. Zhang et al., 2020) in the Aqishan–Yamansu belt, and the abundant Early Permian igneous rocks
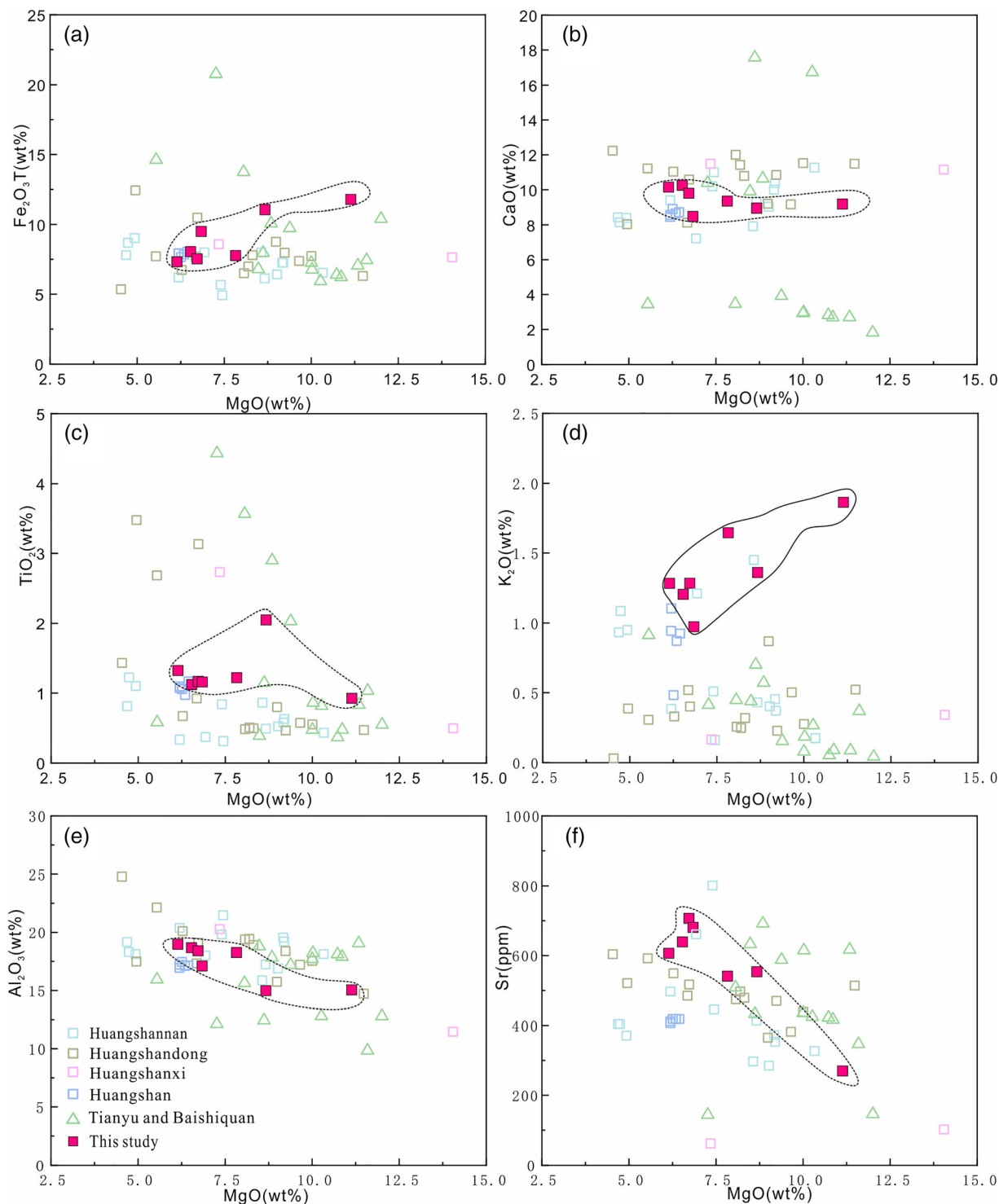
FIGURE 12 (a) Fe_2O_3T, (b) CaO, (c) TiO_2, (d) K_2O, (e) Al_2O_3, and (f) Sr vs. MgO diagrams

with post-collision extensional geochemical features in the Kangguer ductile shear zone and the Central Tianshan Massif (Y. Han & Zhao, 2018; Zhang et al., 2016b), altogether indicate that the Kangguer Oceanic Basin had probably closed by the latest Carboniferous. This is consistent with the occurrence of shear zone-hosted Au deposits at about 300 Ma in the Kangguer belt, which were likely formed during syn-collisional compression (S. Zhang et al., 2020).

Besides, the zircon-rim ages of ca. 303–301 Ma in granites from Yamansu reported by Zhang et al. (2015) were interpreted to have resulted from regional metamorphism associated with arc–continent collision. Thus, the Aqishan–Yamansu Belt is likely in a post-collisional extension setting during the Permian (S. Zhang et al., 2020).

In short, the Permian Shaquanzi mafic intrusions were associated with a post-collisional extensional setting rather than a subduction
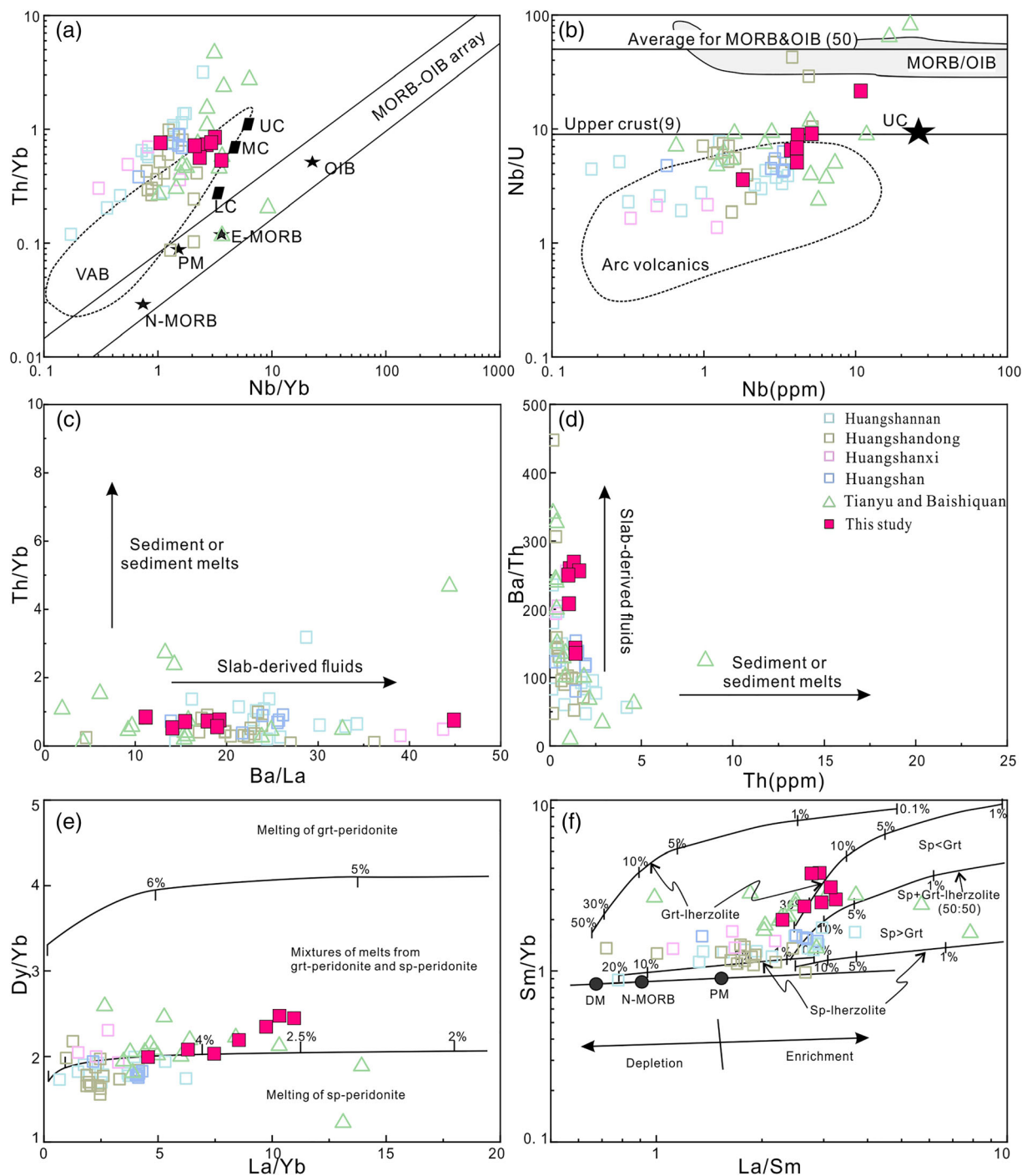
FIGURE 13 (a) Th/Yb vs. Nb/Yb diagram (after Pearce, 2008); (b) Nb/U vs. Nb (after Chung et al., 2001); (c) Th/Yb vs. Ba/La diagram (after Woodhead, Hergt, Davidson, & Eggins, 2001); (d) Ba/Th vs. Th diagram (after Hawkesworth et al., 1997); (e) La/Yb vs. Dy/Yb diagram (after Jung, Jung, Hoffer, & Berndt, 2006); (f) La/Sm vs. Sm/Yb diagram (after Aldanmaz, Pearce, Thirlwall, & Mitchell, 2000). Fields of MORB/OIB and arc volcanics are compiled from Chung et al. (2001)

environment, similar to those proposed for some other Permian mafic-ultramafic intrusions (e.g., Tianyu, Baishiquan, Xiangshan, Huangshan) in the eastern Tianshan (e.g., Deng et al., 2014, 2015, 2020; Mao et al., 2014, Y. J. Mao et al., 2015, 2016; Song et al., 2011; D. Tang et al., 2011, 2013). Partial melting of the metasomatized mantle during the Permian may have been associated with the Tarim mantle plume (J. W. Mao et al., 2008; Su et al., 2011; D. Tang

et al., 2013; M. F. Zhou et al., 2004), and/or asthenospheric upwelling triggered by thickened crustal delamination or slab breakoff (e.g., Y. J. Mao et al., 2016; Song et al., 2011). However, the highly negative Nb–Ta–Ti anomalies and relatively low zircon saturation temperatures (795–848 °C) of the Shaquanzi hornblende gabbro, as well as the lower Ca contents in the olivine from some coeval eastern Tianshan mafic-ultramafic intrusions (Deng et al., 2015), indicate that they differ

FIGURE 14 Tectonic model for the Aqishan–Yamansu Belt in eastern Tianshan during the latest Carboniferous to Early Permian
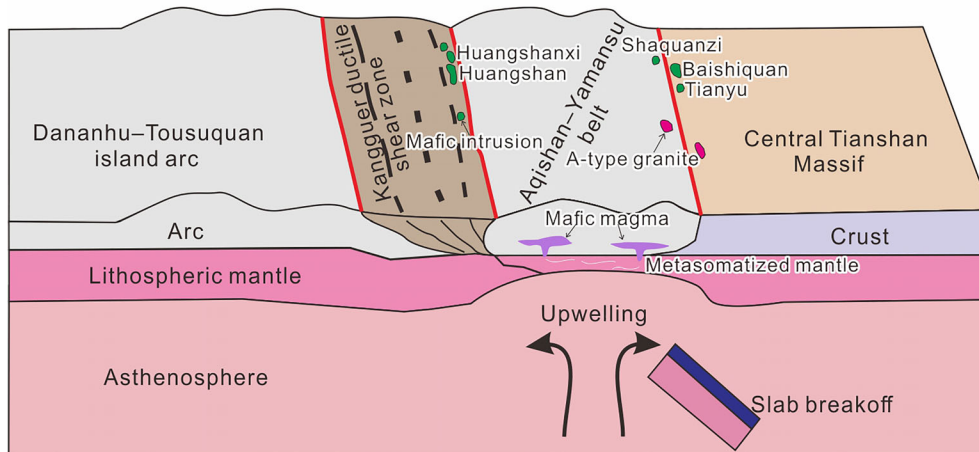
from those of Tarim mantle plume-related basalts (Zhou et al., 2009). Moreover, magmatism formed by thickened crustal delamination would be more-widely distributed. On the contrary, magmatism produced by slab breakoff would likely be more localized and linear (Deng et al., 2015), similar to the narrow, EW-trending mafic-ultramafic magmatic belts in the eastern Tianshan Orogen (Figure 1c; Deng et al., 2015; Yuan et al., 2010). A slab breakoff model is also supported by the spatial proximity and geochemical similarities (incl. Whole-rock geochemistry, Sr–Nd–Pb–Hf isotopes and U–Pb ages) between these Shaquanzi hornblende gabbro samples and the Central Tianshan mafic-ultramafic intrusions (e.g., Baishiquan and Tianyu), which had been clarified to form by slab breakoff in a post-collisional setting (Song et al., 2011; D. Tang et al., 2011). As a result, we propose that the Aqishan–Yamansu Belt was under a post-collisional setting in the latest Carboniferous to Early Permian, and the Permian mafic magma was generated by partial melting of the metasomatized mantle resulted from the slab breakoff (Figure 14).

7 | CONCLUSIONS

1. The Shaquanzi hornblende gabbro in the Aqishan–Yamansu Belt was emplaced at 273.6 ± 2.6 Ma and 265.4 ± 2.2 Ma, around 10–15 Myr after the peak Early Permian mafic-ultramafic plutonism in the eastern Tianshan.
2. The Shaquanzi gabbroic magma was likely sourced from 10 to 30% partial melting of the depleted mantle (garnet- or garnet-spinel-bearing), which may have been metasomatized by slab-derived fluids during the pre-Permian subduction.
3. The Shaquanzi hornblende gabbro is probably the product of extensional-related mafic magmatism (triggered by post-collisional slab breakoff), similar to the generation of many mafic-ultramafic intrusions in the Central Tianshan Massif.

PEER REVIEW

The peer review history for this article is available at https://publons.com/publon/10.1002/gj.4254.

DATA AVAILABILITY STATEMENT

The data that supports the findings of this study are openly available in the tables and supplementary material of this article.

ORCID

Huayong Chen https://orcid.org/0000-0001-9106-9297

REFERENCES

Aldanmaz, E., Pearce, J. A., Thirlwall, M. F., & Mitchell, J. G. (2000). Petrogenetic evolution of late Cenozoic, post-collision volcanism in western Anatolia, Turkey. *Journal of Volcanology and Geothermal Research, 102*, 67–95. https://doi.org/10.1016/S0377-0273(00)00182-7.

Allègre, C. J., & Minster, J. F. (1978). Quantitative models of trace element behavior in magmatic processes. *Earth and Planetary Science Letters, 38*, 1–25. https://doi.org/10.1016/0012-821X(78)90123-1.

Black, L. P., Kamo, S. L., Allen, C. M., Aleinikoff, J. N., Davis, D. W., Korsch, R. J., & Foudoulis, C. (2003). TEMORA 1: a new zircon standard for Phanerozoic U-Pb geochronology. *Chemical Geology, 200*, 155–170. https://doi.org/10.1016/S0009-2541(03)00165-7.

Bouvier, A., Vervoort, J. D., & Patchett, P. J. (2008). The Lu-Hf and Sm-Nd isotopic composition of CHUR: Constraints from unequilibrated chondrites and implications for the bulk composition of terrestrial planets. *Earth and Planetary Science Letters, 273*, 48–57. https://doi.org/10.1016/j.epsl.2008.06.010.

Chai, F., Zhang, Z., Mao, J., Dong, L., Zhang, Z., & Wu, H. (2008). Geology, petrology, and geochemistry of the Baishiquan Ni-Cu-bearing mafic-ultramafic intrusions in Xinjiang, NW China: Implications for tectonics

and genesis of ores. *Journal of Asian Earth Sciences*, 32, 218–235. https://doi.org/10.1016/j.jseaes.2007.10.014.

Charvet, J., Shu, L. S., & Laurent-Charvet, S. (2007). Paleozoic structural and geodynamic evolution of eastern Tianshan (NW China): Welding of the Tarim and Junggar plates. *Episodes*, 30, 162–186.

Chen, B., Yu, J., Liu, S., & Tian, J. (2019). Formation of the Lubei magmatic Ni–Cu deposit in a post-subduction setting in East Tianshan, Northwest China. *Ore Geology Reviews*, 104, 356–372. https://doi.org/10.1016/j.oregeorev.2018.11.017.

Chen, B. Y., Yu, J. J., & Liu, S. J. (2018). Source characteristics and tectonic setting of mafic–ultramafic intrusions in North Xinjiang, NW China: Insights from the petrology and geochemistry of the Lubei mafic–ultramafic intrusion. *Lithos*, 308–309, 329–345. https://doi.org/10.1016/j.lithos.2018.03.016.

Chen, J. P., Wang, H., Liao, Q. A., Zhang, X. H., Luo, T., Wang, J. J., … Liu, X. M. (2016). Geochronological and geochemical of Tudun Cu–Ni-sulphide deposits, East Tianshan. *Geol. Sci. Technol.*, 6, 44–54 (in Chinese with English abstract).

Chen, Y. J., Pirajno, F., Wu, G., Qi, J. P., & Xiong, X. L. (2012). Epithermal deposits in North Xinjiang, NW China. *International Journal of Earth Sciences*, 101, 889–917. https://doi.org/10.1007/s00531-011-0689-4.

Chung, S. L., Wang, K. L., Crawford, A. J., Kamenetsky, V. S., Chen, C. H., Lan, C. Y., & Chen, C. H. (2001). High-Mg potassic rocks from Taiwan: Implications for the genesis of orogenic potassic lavas. *Lithos*, 59, 153–170. https://doi.org/10.1016/S0024-4937(01)00067-6.

Crawford, A. J., Meffre, S., Squire, R. J., Barron, L. M., & Falloon, T. J. (2007). Middle and Late Ordovician magmatic evolution of the Macquarie Arc, Lachlan Orogen, New South Wales. *Australian Journal of Earth Sciences*, 54, 181–214. https://doi.org/10.1080/08120090701227471.

Deng, Y. F., Song, X. Y., Chen, L. M., Zhou, T., Pirajno, F., Yuan, F., … Zhang, D. (2014). Geochemistry of the huangshandong ni-cu deposit in northwestern China: Implications for the formation of magmatic sulphide mineralization in orogenic belts. *Ore Geology Reviews*, 56, 181–198. https://doi.org/10.1016/j.oregeorev.2013.08.012.

Deng, Y. F., Song, X. Y., Hollings, P., Zhou, T., Yuan, F., Chen, L. M., & Zhang, D. (2015). Role of asthenosphere and lithosphere in the genesis of the Early Permian Huangshan mafic-ultramafic intrusion in the Northern Tianshan, NW China. *Lithos*, 227, 241–254. https://doi.org/10.1016/j.lithos.2015.04.014.

Deng, Y. F., Yuan, F., Hollings, P., Song, X. Y., Zhou, T., Fu, B., … Zhao, B. (2020). Magma generation and sulphide saturation of Permian mafic-ultramafic intrusions from the western part of the Northern Tianshan in NW China: Implications for Ni-Cu mineralization. *Mineralium Deposita*, 55, 515–534. https://doi.org/10.1007/s00126-019-00890-8.

Du, L., Long, X., Yuan, C., Zhang, Y., Huang, Z., Wang, X., & Yang, Y. (2018). Mantle contribution and tectonic transition in the Aqishan-Yamansu Belt, Eastern Tianshan, NW China: Insights from geochronology and geochemistry of Early Carboniferous to Early Permian felsic intrusions. *Lithos*, 304–307, 230–244. https://doi.org/10.1016/j.lithos.2018.02.010.

Feng, Y., Qian, Z., Duan, J., Xu, G., Ren, M., & Jiang, C. (2018). Geochronological and geochemical study of the Baixintan magmatic Ni-Cu sulphide deposit: New implications for the exploration potential in the western part of the East Tianshan nickel belt (NW China). *Ore Geology Reviews*, 95, 366–381. https://doi.org/10.1016/j.oregeorev.2018.02.023.

Ferry, J. M., & Watson, E. B. (2007). New thermodynamic models and revised calibrations for the Ti-in-zircon and Zr-in-rutile thermometers. *Contributions to Mineralogy and Petrology*, 154, 429–437. https://doi.org/10.1007/s00410-007-0201-0.

Gao, J. F., & Zhou, M. F. (2013). Generation and evolution of siliceous high magnesium basaltic magmas in the formation of the Permian Huangshandong intrusion (Xinjiang, NW China). *Lithos*, 162–163, 128–139. https://doi.org/10.1016/j.lithos.2013.01.002.

Gao, J. F., Zhou, M. F., Lightfoot, P. C., Wang, C. Y., Qi, L., & Sun, M. (2013). Sulphide saturation and magma emplacement in the formation of the permian huangshandong ni-cu sulphide deposit, Xinjiang, Northwestern China. *Economic Geology*, 108, 1833–1848. https://doi.org/10.2113/econgeo.108.8.1833.

Griffin, W. L., Pearson, N. J., Belousova, E., Jackson, S. E., Van Achterbergh, E., O'Reilly, S. Y., & Shee, S. R. (2000). The Hf isotope composition of cratonic mantle: LAM-MC-ICP-MS analysis of zircon megacrysts in kimberlites. *Geochimica et Cosmochimica Acta*, 64, 133–147. https://doi.org/10.1016/S0016-7037(99)00343-9.

Han, B. F., Ji, J. Q., Song, B., Chen, L. H., & Li Z. H. (2004). SHRIMP zircon U-Pb ages of Kalatongke No. 1 and Huangshandong Cu–Ni-bearing mafic-ultramafic complexes, North Xinjiang, and geological implications. *Chinese Science Bulletin*, 49, 2424–2429.

Han, C., Xiao, W., Zhao, G., Ao, S., Zhang, J., Qu, W., & Du, A. (2010). In-situ U-Pb, Hf and Re-Os isotopic analyses of the Xiangshan Ni-Cu-Co deposit in Eastern Tianshan (Xinjiang), Central Asia Orogenic Belt: Constraints on the timing and genesis of the mineralization. *Lithos*, 120, 547–562. https://doi.org/10.1016/j.lithos.2010.09.019.

Han, C., Xiao, W., Zhao, G., Su, B., Ao, S., Zhang, J., & Wan, B. (2013a). Age and tectonic setting of magmatic sulphide Cu–Ni mineralization in the eastern Tianshan Orogenic Belt, Xinjiang, Central Asia. *Journal of Geosciences (Czech Republic)*, 58, 233–250. https://doi.org/10.3190/jgeosci.148.

Han, C., Xiao, W., Zhao, G., Su, B. X., Sakyi, P. A., Ao, S., … Zhang, Z. (2013b). SIMS U-Pb zircon dating and Re-Os isotopic analysis of the Hulu Cu–Ni deposit, eastern Tianshan, Central Asian Orogenic Belt, and its geological significance. *Journal of Geosciences (Czech Republic)*, 58, 255–274. https://doi.org/10.3190/jgeosci.146.

Han, J. S., Chen, H. Y., Jiang, H. J., Zhao, L. D., Zhang, W. F., & Lai, C. K. (2019). Genesis of the Paleozoic Aqishan-Yamansu Arc-Basin system and Fe (-Cu) mineralization in the Eastern Tianshan, NW China. *Ore Geology Reviews*, 105, 55–70. https://doi.org/10.1016/j.oregeorev.2018.12.012.

Han, Y., & Zhao, G. (2018). Final amalgamation of the Tianshan and Junggar orogenic collage in the southwestern Central Asian Orogenic Belt: Constraints on the closure of the Paleo-Asian Ocean. *Earth-Science Reviews*, 186, 129–152. https://doi.org/10.1016/j.earscirev.2017.09.012.

Hawkesworth, C. J., Turner, S. P., McDermott, F., Peate, D. W., & Van Calsteren, P. (1997). U-Th isotopes in arc magmas: Implications for element transfer from the subducted crust. *Science*, 276(5312), 551–555.

Herzberg, C. (1995). Generation of plume magmas through time: An experimental perspective. *Chemical Geology*, 126, 1–16. https://doi.org/10.1016/0009-2541(95)00099-4.

Hoskin, P. W. O., & Schaltegger, U. (2018). The composition of zircon and igneous and metamorphic petrogenesis. In J. M. Hanchar & P. W. O. Hoskin (Eds.), *Zircon* (pp. 27–62). Berlin, Germany: De Gruyter. https://doi.org/10.1515/9781501509322-005.

Irvine, T. N. (1974). *Petrology of the Duke Island ultramafic complex southern Alaska* (p. 240). Geological Society of America, Memoir 138.

Jahn, B. M., Wu, F., & Chen, B. (2000). Granitoids of the Central Asian Orogenic Belt and continental growth in the Phanerozoic. *Transactions of the Royal Society of Edinburgh, Earth Sciences*, 91, 181–193. https://doi.org/10.1017/s0263593300007367.

Jiang, H., Han, J., Chen, H., Zheng, Y., Lu, W., Deng, G., & Tan, Z. (2017). Intracontinental back-arc basin inversion and Late Carboniferous magmatism in Eastern Tianshan, NW China: Constraints from the Shaquanzi magmatic suite. *Geoscience Frontiers*, 8, 1447–1467. https://doi.org/10.1016/j.gsf.2017.01.008.

Jiang, H., Han, J., Chen, H., Zheng, Y., Zhang, W., Lu, W., … Tan, Z. (2018). Hydrothermal alteration, fluid inclusions and stable isotope characteristics of the Shaquanzi Fe–Cu deposit, Eastern Tianshan: Implications for deposit type and metallogenesis. *Ore Geology Reviews*, 100, 385–400. https://doi.org/10.1016/j.oregeorev.2016.09.025.

Jochum, K. P., Nohl, U., Herwig, K., Lammel, E., Stoll, B., & Hofmann, A. W. (2005). GeoReM: A new geochemical database for reference materials and isotopic standards. *Geostandards and Geoanalytical Research*, *29*, 333–338. https://doi.org/10.1111/j.1751-908X.2005.tb00904.x.

Jung, C., Jung, S., Hoffer, E., & Berndt, J. (2006). Petrogenesis of Tertiary Mafic Alkaline Magmas in the Hocheifel, Germany. *Journal of Petrology*, *47*, 1637–1671. https://doi.org/10.1093/petrology/egl023.

Keppler, H. (1996). Constraints from partitioning experiments on the composition of subduction zone fluids. *Nature*, *380*, 237–240. https://doi.org/10.1038/380237a0.

Koschek, G. (1993). Origin and significance of the SEM cathodoluminescence from zircon. *Journal of Microscopy*, *171*, 223–232. https://doi.org/10.1111/j.1365-2818.1993.tb03379.x.

Li, C. Y., Zhang, H., Wang, F. Y., Liu, J. Q., Sun, Y. L., Hao, X. L., … Sun, W. (2012). The formation of the Dabaoshan porphyry molybdenum deposit induced by slab rollback. *Lithos*, *150*, 101–110. https://doi.org/10.1016/j.lithos.2012.04.001.

Li, D., Wang, Y., Shi, Y., Xie, H., Wang, J., & Lai, C. (2019a). Age and geochemistry of the Carboniferous-Permian magmatism and Fe–Ti–V oxide metallogeny in the Eastern Tianshan Orogen, NW China: Evidence from the Yaxi mafic-ultramafic complex. *International Geology Review*, *61*, 853–867. https://doi.org/10.1080/00206814.2018.1474499.

Li, J. Y., Song, B., Wang, K. Z., Li, Y. P., Sun, G. H., & Qi, D. Y. (2006). Permian mafic-ultramafic complexes on the southern margin of the Tu-Ha Basin, east Tianshan Mountains: Geological records of vertical crustal growth in central Asia. *Acta Geoscientica Sinica*, *27*, 424–446 (in Chinese with English abstract).

Li, W., Cheng, Y., & Yang, Z. (2019b). Geo-*f*O2: Integrated software for analysis of magmatic oxygen fugacity. *Geochemistry, Geophysics, Geosystems*, *20*(5), 2542–2555. https://doi.org/10.1029/2019GC008273.

Li, W. Q., Dong, F. R., & Zhou, R. H. (2000). Ophiolite discovered in Kangurtag region and its characteristics. *Xinjiang Geology*, *18*, 121–128 (in Chinese with English abstract).

Li, X. H., Long, W. G., Li, Q. L., Liu, Y., Zheng, Y. F., Yang, Y. H., … Tao, H. (2010). Penglai zircon megacrysts: A potential new working reference material for microbeam determination of Hf–O isotopes and U–Pb age. *Geostandards and Geoanalytical Research*, *34*, 117–134.

Liu, F., Chai, F., Li, Q., & Yang, F. (2019). Constraints on the timing of Fe–(Cu) metallogenesis in the eastern Aqishan–Yamansu–Shaquanzi metallogenic belt, Eastern Tianshan, NW China. *Ore Geology Reviews*, *113*, 103089. https://doi.org/10.1016/j.oregeorev.2019.103089.

Liu, Y., Gao, S., Hu, Z., Gao, C., Zong, K., & Wang, D. (2010). Continental and oceanic crust recycling-induced melt-peridotite interactions in the Trans-North China Orogen: U-Pb dating, Hf isotopes and trace elements in zircons from mantle xenoliths. *Journal of Petrology*, *51*, 537–571. https://doi.org/10.1093/petrology/egp082.

Long, X., Wu, B., Sun, M., Yuan, C., Xiao, W., & Zuo, R. (2020). Geochronology and geochemistry of Late Carboniferous dykes in the Aqishan–Yamansu belt, eastern Tianshan: Evidence for a post-collisional slab breakoff. *Geoscience Frontiers*, *11*, 347–362. https://doi.org/10.1016/j.gsf.2019.06.003.

Ludwig, K., (2003). *User's manual for Isoplot/Ex version 3.0. A geochronology toolkit for Microsoft Excel, No. 4*. Berkeley Geochronological Centre, Special Publication.

Mao, J., Goldfarb, R. J., Wang, Y., Hart, C. J., Wang, Z., & Yang, J. (2005). Late paleozoic base and precious metal deposits, East Tianshan, Xinjiang, China: Characteristics and geodynamic setting. *Episodes*, *28*, 23–36. https://doi.org/10.18814/epiiugs/2005/v28i1/003.

Mao, J. W., Pirajno, F., Zhang, Z. H., Chai, F. M., Wu, H., Chen, S. P., … Zhang, C. Q. (2008). A review of the Cu–Ni sulphide deposits in the Chinese Tianshan and Altay orogens (Xinjiang Autonomous Region, NW China): Principal characteristics and ore-forming processes. *Journal of Asian Earth Sciences*, *32*, 184–203. https://doi.org/10.1016/j.jseaes.2007.10.006.

Mao, Y. J., Qin, K. Z., Li, C., & Tang, D. M. (2015). A modified genetic model for the Huangshandong magmatic sulphide deposit in the Central Asian Orogenic Belt, Xinjiang, western China. *Mineralium Deposita*, *50*, 65–82. https://doi.org/10.1007/s00126-014-0524-5.

Mao, Y. J., Qin, K. Z., Li, C., Xue, S. C., & Ripley, E. M. (2014). Petrogenesis and ore genesis of the Permian Huangshanxi sulphide ore-bearing mafic-ultramafic intrusion in the Central Asian Orogenic Belt, western China. *Lithos*, *200–201*, 111–125. https://doi.org/10.1016/j.lithos.2014.04.008.

Mao, Y. J., Qin, K. Z., Tang, D. M., Feng, H. Y., & Xue, S. C. (2016). Crustal contamination and sulphide immiscibility history of the Permian Huangshannan magmatic Ni-Cu sulphide deposit, East Tianshan, NW China. *Journal of Asian Earth Sciences*, *129*, 22–37. https://doi.org/10.1016/j.jseaes.2016.07.028.

Middlemost, E. A. K. (1994). Naming materials in the magma/igneous rock system. *Earth-Science Reviews*, *37*, 215–224. https://doi.org/10.1016/0012-8252(94)90029-9.

Pearce, J. A. (2008). Geochemical fingerprinting of oceanic basalts with applications to ophiolite classification and the search for Archean oceanic crust. *Lithos*, *100*, 14–48. https://doi.org/10.1016/j.lithos.2007.06.016.

Pearce, J. A., Stern, R. J., Bloomer, S. H., & Fryer, P. (2005). Geochemical mapping of the Mariana Arc-Basin system: Implications for the nature and distribution of subduction components. *Geochemistry, Geophysics, Geosystems*, *6*(7), 1–27. https://doi.org/10.1029/2004GC000895.

Pearce, N. J. G., Perkins, W. T., Westgate, J. A., Gorton, M. P., Jackson, S. E., Neal, C. R., & Chenery, S. P. (1997). A compilation of new and published major and trace element data for NIST SRM 610 and NIST SRM 612 glass reference materials. *Geostandards Newsletter*, *21*, 115–144. https://doi.org/10.1111/j.1751-908X.1997.tb00538.x.

Peccerillo, A., & Taylor, S. R. (1976). Geochemistry of eocene calc-alkaline volcanic rocks from the Kastamonu area, Northern Turkey. *Contributions to Mineralogy and Petrology*, *58*, 63–81. https://doi.org/10.1007/BF00384745.

Polat, A., & Hofmann, A. W. (2003). Alteration and geochemical patterns in the 3.7–3.8 Ga Isua greenstone belt, West Greenland. *Precambrian Research*, *126*, 197–218. https://doi.org/10.1016/S0301-9268(03)00095-0.

Qian, Y., Ge, W. C., Yang, H., Zhao, G. C., Zhang, Y. L., & Su, L. (2014). Petrogenesis of late Paleozoic volcanic rocks from the Daheshen Formation in central Jilin Province, NE China, and its tectonic implications: constraints from geochronology, geochemistry, and Sr–Nd–Hf isotopes. *Lithos*, *192*, 116–131. https://doi.org/10.1016/j.lithos.2014.01.016.

Qin, K. Z., Fang, T. H., Wang, S. L., Zhu, B. Q., Feng, Y. M., Yu, H. F., & Xiu, Q. Y. (2002). Plate tectonics division, evolution and metallogenic settings in eastern Tianshan mountains, NW China. *Xinjiang Geology*, *20*, 302–308 (in Chinese with English abstract).

Qin, K. Z., Su, B. X., Sakyi, P. A., Tang, D. M., Li, X. H., Sun, H., … Liu, P. P. (2011). Sims zircon U-Pb geochronology and Sr–Nd isotopes of Ni-Cu-bearing mafic-ultramafic intrusions in Eastern Tianshan and beishan in correlation with flood basalts in Tarim Basin (NW China): Constraints on a CA. 280 MA mantle plume. *American Journal of Science*, *311*, 237–260. https://doi.org/10.2475/03.2011.03.

Qin, K. Z., Tang, D. M., Su, B. X., Mao, Y. J., Xue, S. C., Tian, Y., … Deng, G. (2012). The Tectonic setting, style, basic feature, relative erosion deee, ore-bearing evaluation sign, potential analysis of mineralization of Cu-Ni-bearing Permian mafic-ultramafic complexes, northern Xinjiang. *Northwestern Geology*, *45*(4), 83–116 (in Chinese with English abstract).

Robinson, J. A. C., & Wood, B. J. (1998). The depth of the spinel to garnet transition at the peridotite solidus. *Earth and Planetary Science Letters*, *164*, 277–284. https://doi.org/10.1016/S0012-821X(98)00213-1.

Rogers, N., Macdonald, R., Fitton, J. G., George, R., Smith, M., & Barreiro, B. (2000). Two mantle plumes beneath the east African rift system: Sr, Nd and Pb isotope evidence from Kenya Rift basalts. *Earth and Planetary Science Letters*, *176*, 387–400.

Rudnick, R. L., & Fountain, D. M. (1995). Nature and composition of the continental crust: A lower crustal perspective. *Reviews of Geophysics*, *33*(3), 267–309. https://doi.org/10.1029/95RG01302.

San, J. Z., Qin, K. Z., Tang, Z. L., Tang, D. M., Su, B. X., Sun, H., ... Liu, P. P. (2010). Precise zircon U-Pb age dating of two mafic-ultramafic complexes at Tulargen large Cu–Ni district and its geological implications. *Acta Petrologica Sinica*, *26*, 3027–3035 (in Chinese with English abstract).

Schiano, P., Monzier, M., Eissen, J. P., Martin, H., & Koga, K. T. (2010). Simple mixing as the major control of the evolution of volcanic suites in the Ecuadorian Andes. *Contributions to Mineralogy and Petrology*, *160*, 297–312.

Şengör, A. M. C., Natal'In, B. A., & Burtman, V. S. (1993). Evolution of the Altaid tectonic collage and Palaeozoic crustal growth in Eurasia. *Nature*, *364*, 299–307. https://doi.org/10.1038/364299a0.

Shi, Y., Wang, Y., Wang, J., Zhao, L., Xie, H., Long, L., ... Zhou, G. (2018). Physicochemical control of the Early Permian Xiangshan Fe–Ti oxide deposit in Eastern Tianshan (Xinjiang), NW China. *Journal of Earth Science*, *29*, 520–536. https://doi.org/10.1007/s12583-017-0969-4.

Shi, Y., Wang, Y., Wang, J., Zhou, G., Xie, H., Li, D., ... Tang, H. (2021). Formation of the Weiya magmatic Fe–Ti oxide deposit and its ore-hosting layered gabbro intrusion, Eastern Tianshan (Xinjiang, NW China). *Ore Geology Reviews*, *132*, 104003. https://doi.org/10.1016/j.oregeorev.2021.104003.

Söderlund, U., Patchett, P. J., Vervoort, J. D., & Isachsen, C. E. (2004). The 176Lu decay constant determined by Lu–Hf and U-Pb isotope systematics of Precambrian mafic intrusions. *Earth and Planetary Science Letters*, *219*, 311–324. https://doi.org/10.1016/S0012-821X(04)00012-3.

Song, X. Y., & Li, X. R. (2009). Geochemistry of the Kalatongke Ni-Cu-(PGE) sulfide deposit, NW China: Implications for the formation of magmatic sulfide mineralization in a postcollisional environment. *Mineralium Deposita*, *44*, 303–327. https://doi.org/10.1007/s00126-008-0219-x.

Song, X. Y., Xie, W., Deng, Y. F., Crawford, A. J., Zheng, W. Q., Zhou, G. F., ... Li, J. (2011). Slab breakoff and the formation of Permian mafic-ultramafic intrusions in southern margin of Central Asian Orogenic Belt, Xinjiang, NW China. *Lithos*, *127*, 128–143. https://doi.org/10.1016/j.lithos.2011.08.011.

Su, B. X., Qin, K. Z., Sakyi, P. A., Li, X. H., Yang, Y. H., Sun, H., ... Malaviarachchi, S. P. K. (2011). U-pb ages and hf-o isotopes of zircons from late paleozoic mafic-ultramafic units in the southern central asian orogenic belt: Tectonic implications and evidence for an early permian mantle plume. *Gondwana Research*, *20*, 516–531. https://doi.org/10.1016/j.gr.2010.11.015.

Su, B. X., Qin, K. Z., Sun, H., Tang, D. M., Sakyi, P. A., Chu, Z. Y., ... Xiao, Q. H. (2012). Subduction-induced mantle heterogeneity beneath Eastern Tianshan and Beishan: Insights from Nd-Sr-Hf-O isotopic mapping of Late Paleozoic mafic-ultramafic complexes. *Lithos*, *134–135*, 41–51. https://doi.org/10.1016/j.lithos.2011.12.011.

Su, B. X., Qin, K. Z., Zhou, M. F., Sakyi, P. A., Thakurta, J., Tang, D. M., ... Sun, H. (2014). Petrological, geochemical and geochronological constraints on the origin of the Xiadong Ural-Alaskan-type complex in NW China and tectonic implication for the evolution of southern Central Asian Orogenic Belt. *Lithos*, *200–201*, 226–240. https://doi.org/10.1016/j.lithos.2014.05.005.

Sun, S. S., & McDonough, W. F. (1989). Chemical and isotopic systematics of oceanic basalts: Implications for mantle composition and processes. *Geological Society, London, Special Publications*, *42*, 313–345. https://doi.org/10.1144/GSL.SP.1989.042.01.19.

Sun, T., Qian, Z. Z., Deng, Y. F., Li, C., Song, X. Y., & Tang, Q. (2013a). PGE and isotope (Hf-Sr-Nd–Pb) constraints on the origin of the Huangshandong magmatic Ni-Cu sulphide deposit in the Central Asian Orogenic Belt, Northwestern China. *Economic Geology*, *108*, 1849–1864. https://doi.org/10.2113/econgeo.108.8.1849.

Sun, T., Qian, Z. Z., Li, C., Xia, M. Z., & Yang, S. H. (2013b). Petrogenesis and economic potential of the Erhongwa mafic-ultramafic intrusion in the Central Asian Orogenic Belt, NW China: Constraints from olivine chemistry, U-Pb age and Hf isotopes of zircons, and whole-rock Sr–Nd–Pb isotopes. *Lithos*, *182–183*, 185–199. https://doi.org/10.1016/j.lithos.2013.10.004.

Sun, W., Hu, Y., Kamenetsky, V. S., Eggins, S. M., Chen, M., & Arculus, R. J. (2008). Constancy of Nb/U in the mantle revisited. *Geochimica et Cosmochimica Acta*, *72*, 3542–3549. https://doi.org/10.1016/j.gca.2008.04.029.

Sun, Y., Wang, J., Lv, X., Yu, M., Li, Y., Mao, Q., ... Long, L. (2019). Geochronology, petrogenesis and tectonic implications of the newly discovered Cu–Ni sulphide-mineralized Yueyawan gabbroic complex, Kalatag district, northwestern Eastern Tianshan, NW China. *Ore Geology Reviews*, *109*, 598–614. https://doi.org/10.1016/j.oregeorev.2019.05.009.

Tang, D., Qin, K., Li, C., Qi, L., Su, B., & Qu, W. (2011). Zircon dating, Hf-Sr–Nd-Os isotopes and PGE geochemistry of the Tianyu sulphide-bearing mafic-ultramafic intrusion in the Central Asian Orogenic Belt, NW China. *Lithos*, *126*, 84–98. https://doi.org/10.1016/j.lithos.2011.06.007.

Tang, D., Qin, K., Su, B., Sakyi, P. A., Liu, Y., Mao, Q., ... Ma, Y. (2013). Magma source and tectonics of the Xiangshanzhong mafic-ultramafic intrusion in the Central Asian Orogenic Belt, NW China, traced from geochemical and isotopic signatures. *Lithos*, *170–171*, 144–163. https://doi.org/10.1016/j.lithos.2013.02.013.

Tang, D. M., Qin, K. Z., Sun, H., Su, B. X., Xiao, Q. H., Cheng, S. L., & Li, J. (2009). Zircon U-Pb age and geochemical characteristics of Tianyu intrusion, East Tianshan: Constraints on source and genesis of mafic-ultramafic intrusions in East Xinjiang. *Acta Petrologica Sinica*, *25*, 817–831 (in Chinese with English abstract).

Tang, G. J., Wang, Q., Wyman, D. A., Li, Z. X., Zhao, Z. H., & Yang, Y. H. (2012). Late carboniferous high εNd(t)–εHf(t) granitoids, enclaves, and dikes in western Junggar, NW China: ridge-subduction-related magmatism and crustal growth. *Lithos*, *140–141*, 86–102.

Wang, H., Wu, Y. B., Qin, Z. W., Zhu, L. Q., Liu, Q., Liu, X. C., ... Yuan, H. L. (2013). Age and geochemistry of Silurian gabbroic rocks in the Tongbai orogen, central China: Implications for the geodynamic evolution of the North Qinling arc-back-arc system. *Lithos*, *179*, 1–15. https://doi.org/10.1016/j.lithos.2013.07.021.

Wang, Y. W., Wang, J. B., Wang, L. J., & Long, L. L. (2009). Characteristics of two mafic-ultramafic rock series in the Xiangshan Cu–Ni-(V) Ti–Fe ore district, Xinjiang. *Acta Petrologica Sinica*, *25*, 888–900 (in Chinese with English abstract).

Watson, E. B. (1982). Basalt contamination by continental crust: Some experiments and models. *Contributions to Mineralogy and Petrology*, *80*, 73–87. https://doi.org/10.1007/BF00376736.

Watson, E. B., Wark, D. A., & Thomas, J. B. (2006). Crystallization thermometers for zircon and rutile. *Contributions to Mineralogy and Petrology*, *151*, 413–433. https://doi.org/10.1007/s00410-006-0068-5.

Wilson, M. (1989). *Igneous petrogenesis*. London, England: Springer, Harper Collins Academic.

Winchester, J. A., & Floyd, P. A. (1977). Geochemical discrimination of different magma series and their differentiation products using immobile elements. *Chemical Geology*, *20*, 325–343. https://doi.org/10.1016/0009-2541(77)90057-2.

Windley, B. F., Alexeiev, D., Xiao, W., Kröner, A., & Badarch, G. (2007). Tectonic models for accretion of the Central Asian Orogenic Belt. *Journal of the Geological Society*, *164*, 31–47. https://doi.org/10.1144/0016-76492006-022.

Woodhead, J. D., Hergt, J. M., Davidson, J. P., & Eggins, S. M. (2001). Hafnium isotope evidence for "conservative" element mobility during

subduction zone processes. *Earth and Planetary Science Letters*, 192, 331–346. https://doi.org/10.1016/S0012-821X(01)00453-8.

Wu, B., (2019). *Late paleozoic magmatism and crustal growth in the Aqishan-Yamansu Belt of Eastern Tianshan* (MS thesis). Xi'an, China, North-west University (in Chinese with English abstract).

Wu, H., Li, H. Q., Mo, X. H., Chen, F. W., Lu, Y. F., Mei, Y. P., & Deng, G. (2005). Age of the Baishiquan mafic-ultramafic complex, Hami, Xinjiang and its geological significance. *Acta Petrologica Sinica*, 79, 498–502 (in Chinese with English abstract).

Xia, M. Z., Jiang, C. Y., Qian, Z. Z., Sun, T., Xia, Z. D., & Lu, R. H. (2008). Geochemistry and petrogenesis for Hulu intrusion in East Tianshan, Xinjiang. *Acta Petrologica Sinica*, 24, 2749–2760 (in Chinese with English abstract).

Xiao, B., Chen, H., Hollings, P., Han, J., Wang, Y., Yang, J., & Cai, K. (2017). Magmatic evolution of the Tuwu–Yandong porphyry Cu belt, NW China: Constraints from geochronology, geochemistry and Sr–Nd–Hf isotopes. *Gondwana Research*, 43, 74–91. https://doi.org/10.1016/j.gr.2015.09.003.

Xiao, W., Han, C., Liu, W., Wan, B., Zhang, J., Ao, S., ... Luo, J. (2014). How many sutures in the southern Central Asian Orogenic Belt: Insights from East Xinjiang-West Gansu (NW China)? *Geoscience Frontiers*, 5, 525–536. https://doi.org/10.1016/j.gsf.2014.04.002.

Xiao, W., Windley, B. F., Allen, M. B., & Han, C. (2013). Paleozoic multiple accretionary and collisional tectonics of the Chinese Tianshan orogenic collage. *Gondwana Research*, 23, 1316–1341. https://doi.org/10.1016/j.gr.2012.01.012.

Xiao, W. J., Windley, B. F., Sun, S., Li, J. L., Huang, B. C., Han, C. M., ... Chen, H. L. (2015). A tale of amalgamation of three permo-triassic collage systems in central Asia: Oroclines, sutures, and terminal accretion. *Annual Review of Earth and Planetary Sciences*, 43, 16.1–16.31. https://doi.org/10.1146/annurev-earth-060614-105254.

Xiao, W. J., Zhang, L. C., Qin, K. Z., Sun, S., & Li, J. L. (2004). Paleozoic accretionary and collisional tectonics of the Eastern Tianshan (China): Implications for the continental growth of central Asia. *American Journal of Science*, 304, 370–395. https://doi.org/10.2475/ajs.304.4.370.

Xu, Y. G., Zhang, H. H., Qiu, H. N., Ge, W. C., & Wu, F. Y. (2012). Oceanic crust components in continental basalts from Shuangliao, North-east China: Derived from the mantle transition zone? *Chemical Geology*, 328, 168–184. https://doi.org/10.1016/j.chemgeo.2012.01.027.

Yan, S., Shan, Q., Niu, H. C., Yang, W. B., Li, N. B., Zeng, L. J., & Jiang, Y. H. (2015). Petrology and geochemistry of late Carboniferous hornblende gabbro from the Awulale Mountains, western Tianshan (NW China): Implication for an arc-nascent back-arc environment. *Journal of Asian Earth Sciences*, 113, 218–237. https://doi.org/10.1016/j.jseaes.2015.01.016.

Yuan, C., Sun, M., Wilde, S., Xiao, W., Xu, Y., Long, X., & Zhao, G. (2010). Post-collisional plutons in the Balikun area, East Chinese Tianshan: Evolving magmatism in response to extension and slab breakoff. *Lithos*, 119, 269–288. https://doi.org/10.1016/j.lithos.2010.07.004.

Zhang, D. Y. (2012). *Petrogenesis, mineralization and geodynamic evolution in Jueluotage Area, Eastern Tianshan, North-west China* (PhD thesis). Hefei, China: Hefei University of Technology (in Chinese with English abstract).

Zhang, S., Chen, H., Hollings, P., Zhao, L., & Gong, L. (2020). Tectonic and magmatic evolution of the Aqishan-Yamansu belt: A Paleozoic arc-related basin in the Eastern Tianshan (NW China). *GSA Bulletin*, 133, 1320–1344. https://doi.org/10.1130/b35749.1.

Zhang, W., Chen, H., Han, J., Zhao, L., Huang, J., Yang, J., & Yan, X. (2016a). Geochronology and geochemistry of igneous rocks in the Bailingshan area: Implications for the tectonic setting of late Paleozoic magmatism and iron skarn mineralization in the eastern Tianshan, NW

China. *Gondwana Research*, 38, 40–59. https://doi.org/10.1016/j.gr.2015.10.011.

Zhang, W., Chen, H., Jiang, H., Lu, W., Liang, P., Xu, C., ... Yang, J. (2017). Geochronology, geochemistry and petrogenesis of granitoids in the Duotoushan Fe-Cu deposit, Eastern Tianshan, Xinjiang Province: Implications on tectonic setting of late Paleozoic magmatism. *Geotectonica et Metallogenia*, 14, 1171–1191 (in Chinese with English abstract).

Zhang, W., Chen, H., Peng, L., Zhao, L., Huang, J., Lu, W., ... Lai, C. (2018). Discriminating hydrothermal fluid sources using tourmaline boron isotopes: Example from Bailingshan Fe deposit in the Eastern Tianshan, NW China. *Ore Geology Reviews*, 98, 28–37. https://doi.org/10.1016/j.oregeorev.2018.05.015.

Zhang, X., Zhao, G., Eizenhöfer, P. R., Sun, M., Han, Y., Hou, W., ... Xu, B. (2015). Latest Carboniferous closure of the Junggar Ocean constrained by geochemical and zircon U–Pb–Hf isotopic data of granitic gneisses from the Central Tianshan block, NW China. *Lithos*, 238, 26–36.

Zhang, X., Zhao, G., Eizenhöfer, P. R., Sun, M., Han, Y., Hou, W., ... Zhu, C. Y. (2016b). Tectonic transition from Late Carboniferous subduction to Early Permian post-collisional extension in the Eastern Tianshan, NW China: Insights from geochronology and geochemistry of mafic-intermediate intrusions. *Lithos*, 256–257, 269–281. https://doi.org/10.1016/j.lithos.2016.04.006.

Zhao, J. H., & Zhou, M. F. (2007). Geochemistry of Neoproterozoic mafic intrusions in the Panzhihua district (Sichuan Province, SW China): Implications for subduction-related metasomatism in the upper mantle. *Precambrian Research*, 152, 27–47. https://doi.org/10.1016/j.precamres.2006.09.002.

Zhao, J. H., & Zhou, M. F. (2009). Secular evolution of the Neoproterozoic lithospheric mantle underneath the northern margin of the Yangtze Block, South China. *Lithos*, 107, 152–168. https://doi.org/10.1016/j.lithos.2008.09.017.

Zhao, L., Chen, H., Hollings, P., & Han, J. (2019a). Tectonic transition in the Aqishan-Yamansu belt, Eastern Tianshan: Constraints from the geochronology and geochemistry of Carboniferous and Triassic igneous rocks. *Lithos*, 344–345, 247–264. https://doi.org/10.1016/j.lithos.2019.06.023.

Zhao, L., Chen, H., Hollings, P., & Han, J. (2019b). Late Paleozoic magmatism and metallogenesis in the Aqishan-Yamansu belt, Eastern Tianshan: Constraints from the Bailingshan intrusive complex. *Gondwana Research*, 65, 68–85. https://doi.org/10.1016/j.gr.2018.08.004.

Zhao, L., Chen, H., Zhang, L., Zhang, W., Yang, J., & Yan, X. (2018b). The Late Paleozoic magmatic evolution of the Aqishan-Yamansu belt, Eastern Tianshan: Constraints from geochronology, geochemistry and Sr–Nd–Pb–Hf isotopes of igneous rocks. *Journal of Asian Earth Sciences*, 153, 170–192. https://doi.org/10.1016/j.jseaes.2017.07.038.

Zhao, Y., Xue, C., Symons, D. T. A., Zhao, X., Zhang, G., Yang, Y., & Zu, B. (2018a). Temporal variations in the mantle source beneath the Eastern Tianshan nickel belt and implications for Ni–Cu mineralization potential. *Lithos*, 314–315, 597–616. https://doi.org/10.1016/j.lithos.2018.06.011.

Zhao, Y., Xue, C., Zhao, X., Yang, Y. Q., & Ke, J. (2015). Magmatic Cu–Ni sulphide mineralization of the Huangshannan mafic-untramafic intrusion, Eastern Tianshan, China. *Journal of Asian Earth Sciences*, 105, 155–172. https://doi.org/10.1016/j.jseaes.2015.03.031.

Zhou, G. C., Wang, Y. W., Shi, Y., Xie, H. J., Li, D. D., & Guo, B. R. (2019). Geochronology and geochemistry of mafic intrusions in the Kalatag area, eastern Tianshan. *Acta Petrologica Sinica*, 35, 3189–3212 (in Chinese with English abstract).

Zhou, M. F., Lesher, C. M., Yang, Z., Li, J., & Sun, M. (2004). Geochemistry and petrogenesis of 270 Ma Ni-Cu-(PGE) sulphide-bearing mafic intrusions in the Huangshan district, Eastern Xinjiang, North-west China:

Implications for the tectonic evolution of the Central Asian orogenic belt. *Chemical Geology*, *209*, 233–257. https://doi.org/10.1016/j.chemgeo.2004.05.005.

Zhou, T. F., Yuan, F., Zhang, D., Fan, Y., Liu, S., Peng, M., & Zhang, J. (2010). Geochronology, tectonic setting and mineralization of granitoids in Jueluotage area, Eastern Tianshan, Xinjiang. *Acta Petrologica Sinica*, *26*, 478–502 (in Chinese with English abstract).

Zhou, M. F., Zhao, J. H., Jiang, C. Y., Gao, J. F., Wang, W., & Yang, S. H. (2009). OIB-like, heterogeneous mantle sources of Permian basaltic magmatism in the western Tarim Basin, NW China: implications for a possible Permian large igneous province. *Lithos*, *113*(3-4), 583–594.

Zindler, A., & Hart, S. (1986). Chemical geodynamics. *Annual Review of Earth and Planetary Sciences*, *14*, 493–571.

SUPPORTING INFORMATION

Additional supporting information may be found in the online version of the article at the publisher's website.